Rochester Institute of Technology
RIT Scholar Works

Theses | Thesis/Dissertation Collections

12-1-2009

VHF-UHF passive filter synthesis based on acoustic resonator structures

Melissa Sefton Dempsey

Follow this and additional works at: http://scholarworks.rit.edu/theses

Recommended Citation
Dempsey, Melissa Sefton, "VHF-UHF passive filter synthesis based on acoustic resonator structures" (2009). Thesis. Rochester Institute of Technology. Accessed from

This Thesis is brought to you for free and open access by the Thesis/Dissertation Collections at RIT Scholar Works. It has been accepted for inclusion in Theses by an authorized administrator of RIT Scholar Works. For more information, please contact ritscholarworks@rit.edu.

VHF-UHF Passive Filter Synthesis Based on Acoustic Resonator Structures

by

Melissa Sefton Dempsey

A Thesis Submitted in Partial Fulfillment of the

Requirements for the Degree of

Master of Science

in

Electrical and Microelectronic Engineering

Approved by:

_____

Advisor: Dr. Robert J. Bowman

_____

Member: Dr. Karl D. Hirschman

_____

Member: Dr. James E. Moon

_____

Department Head: Dr. Sohail A. Dianat

Department of Electrical Engineering

Kate Gleason College of Engineering

Rochester Institute of Technology

Rochester, New York

December 2009

Acknowledgements

I would like to give thanks to my advisor, Dr. Robert Bowman, whose knowledge, guidance and patience has made my graduate experience extremely rewarding. Having been both a graduate research assistant and a student of many of his courses, I am grateful for his deep insight and skill in many areas (e.g. circuit analysis, electronic circuit design, filter design, analog and mixed-signal IC design). I would like to thank the other members of the committee, Dr. Karl Hirschman and Dr. James Moon for their time and effort spent in understanding my research.

A very special thanks goes out to Dr. Joseph Revelli, whose extensive support and encouragement has helped make my research a success. I am extremely lucky to have worked with and learned from someone with such a thorough understanding of so many topics. Specifically, he has assisted me in understanding the physics of surface acoustic wave devices. His methodical attention to detail has been a great inspiration to me during my research experience, and will continue to inspire me in my professional career. I will miss having such a distinguished and intelligent person in my midst.

I would like to thank my family and friends for their continuous support. I am especially appreciative of my parents, whose love and understanding has helped me throughout my life.

Last of all, this research would not have been possible without the financial assistance of PPC. I would especially like to thank Noah Montena, Michael Lawrence and Erdogan Alkan for useful discussions that helped me greatly in my research.

Abstract

This thesis presents a novel design method for approximating standard bandpass filter transfer functions using surface acoustic wave (SAW) technology. This method is based on standard circuit simulation and optimization tools to generate physical specifications for the fabrication of a SAW impedance element filter (IEF) network. The IEF topology is verified in the design of a narrowband bandpass filter composed of commercial quartz SAW resonators. The utility of the design method is further demonstrated for a wider bandwidth filter based on custom resonators fabricated on a lithium niobate substrate. An optimum fit was obtained between the standard filter target response and the corresponding SAW IEF response. Comparisons made between the two networks show that by exploiting the high *Q* characteristics of SAW devices in an IEF configuration, smaller footprints and tighter filter tolerances are obtained.

Table of Contents

List of Abbreviations

BAW	Bulk Acoustic Wave
BVD	Butterworth Van-Dyke
IDT	Interdigital Transducer
IEF	Impedance Element Filter
IIDT	Interdigitated Interdigital Transducer
SAW	Surface Acoustic Wave
TCRF	Transverse-Coupled Resonator Filter

List of Tables

List of Figures

1 Introduction

1.1 Passive Filters in VHF and UHF

Passive filters are essential components in a vast array of electronic systems. By definition, networks consisting only of passive filters contain no active elements and do not require an external power supply. They have become increasingly important to the development of television, cellular and satellite radio components. These devices typically operate in the VHF (30-300 MHz) and UHF (300-3000 MHz) frequency ranges. Consequently, advancement of VHF and UHF passive filter designs for signal processing has become a crucial topic. There are four main types of filter passive responses: lowpass, highpass, bandpass and bandstop. This work focuses on bandpass filters.

There are many metrics which specify a filter's performance. These are illustrated in Figure 1-1. In the case of bandpass filters, passband ripple is a measure of the flatness of the filter response. It is measured as the difference between the highest and lowest insertion loss value between the two passband edges. Stopband attenuation is the difference in attenuation between the passband and stopband edges. It is a measure of the degree to which a filter attenuates signals at certain frequencies. In bandpass filters, skirt steepness is a ratio of passband and stopband bandwidths (in bandstop filters, it is the reciprocal). As shown in Figure 1-1, the stopband bandwidth is the sum of the passband bandwidth and the two transition bands [1].

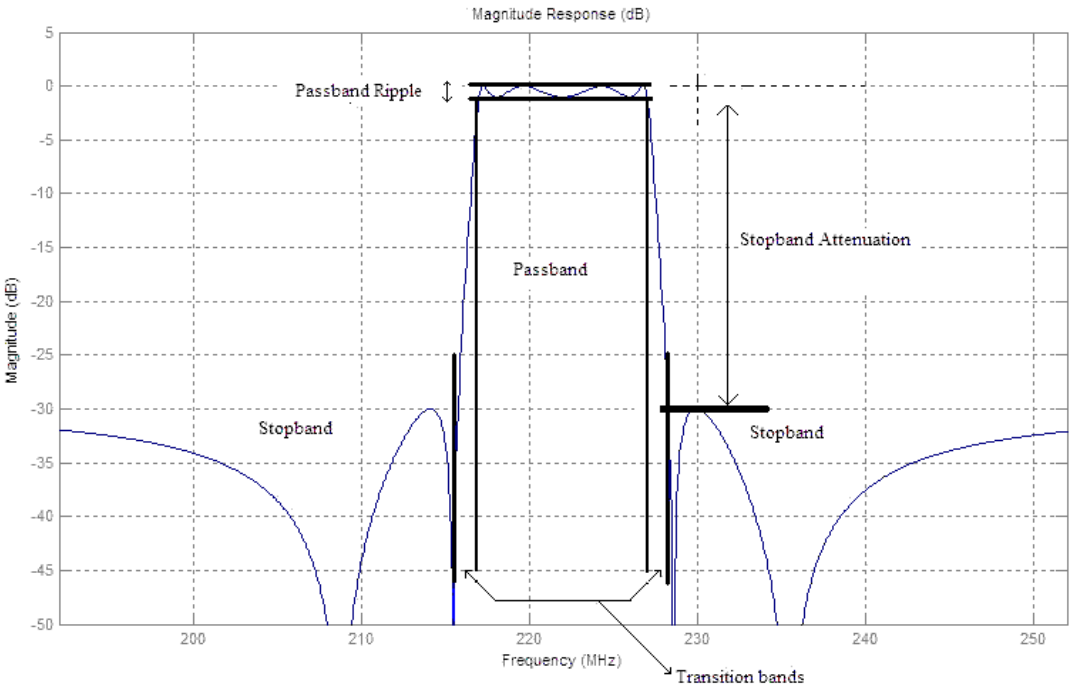

Figure 1-1: Specifications for a bandpass filter. Adapted from [2]

One of the most significant figures of merit for any filter is its quality factor, *Q*. This is defined as the ratio of the filter center frequency to the bandwidth, shown in (1-1).

$$Q = \frac{f_o}{BW} \tag{1-1}$$

where the center frequency is equal to the geometric mean of the two passband edge frequencies (for bandpass filters).

1.2 *LC* Passive Network Topologies

LC passive filter design is a very mature discipline dating back almost a century. Seminal work in the development of *LC* filters includes Heaviside's studies on lumped loading [3], Campbell and Wagner's simultaneous discovery of the *LC* lowpass ladder

filter [4] [5], and Otto Zobel's theory involving cascaded filter sections [6]. Development in this subject has led to *LC* ladder and lattice networks that realize high performance filter responses. These filters offer stability, linearity, low noise and portability at relatively low cost [7].

1.2.1 *LC* Ladder Filters

A filter approximation is typically described using a network function. This function of complex frequency is represented as a ratio of polynomials with the order of the filter approximation being the highest power in the denominator polynomial. When filter approximations of high order are required, passive *LC* ladder networks are among the least sensitive and best performing topologies. *LC* ladder filters have alternating series and shunt branches comprised of inductors and capacitors. They are based on two-port lowpass prototype networks designed to operate from a 1Ω generator into an equal load. A typical lowpass prototype is shown in Figure 1-2.

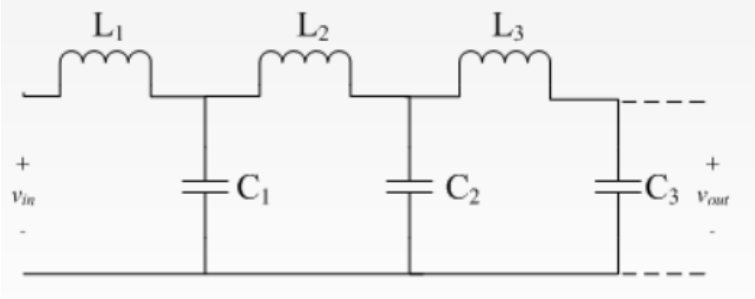

Figure 1-2 : Conventional *LC* two-port lowpass prototype.

Conventional ladder filter design begins with fitting a standard filter approximation (Butterworth, Chebyshev, and Elliptic) to a lowpass prototype (similar to Figure 1-2). The abundance of computer-generated tables helps in creating high performance

prototypes. Usually, lowpass circuit component values are referenced by the desired filter order and attenuation characteristics needed, and are normalized to 1 radian per second.

Once a lowpass prototype network is specified it can then be transformed into a different filter type- *i.e.* highpass, bandpass, bandstop. This transformation involves adding inductors and capacitors in order to realize the desired transfer function. For example, a lowpass to bandpass transformation entails adding parallel inductors to shunt-branch capacitors and series capacitors to series-branch inductors. The figure below represents the standard configuration of a bandpass *LC* ladder filter.

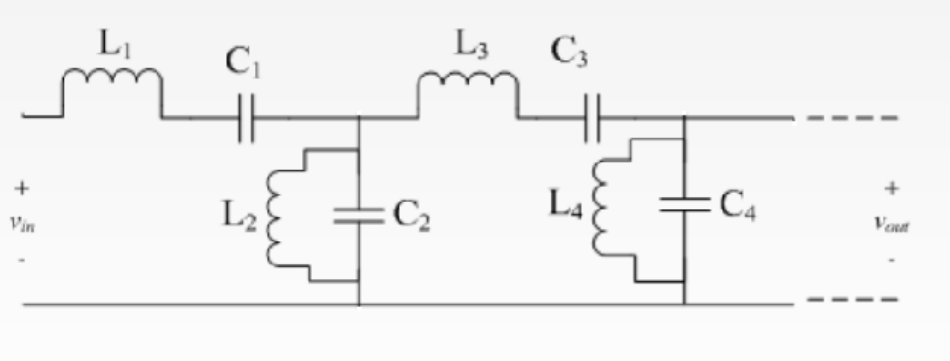

Figure 1-3 : Standard configuration of a bandpass *LC* ladder filter.

After the prototype is transformed to a chosen response, it must be frequency and impedance denormalized. That is, the inductors in the circuit are multiplied by the transmission line impedance while the capacitors are divided by it. In addition, the capacitors and inductors in the circuit are divided by the center frequency of the filter.

1.2.2 An Example of a High Performance *LC* Ladder Prototype Filter

A high *Q* bandstop filter design is illustrated in Figure 1-4. A 15^{th} order elliptic filter function is chosen using tabulated values for a normalized lowpass *LC* ladder filter

that meets specifications. The bandstop filter can be realized using standard filter transformation techniques between lowpass and bandstop filter approximations.

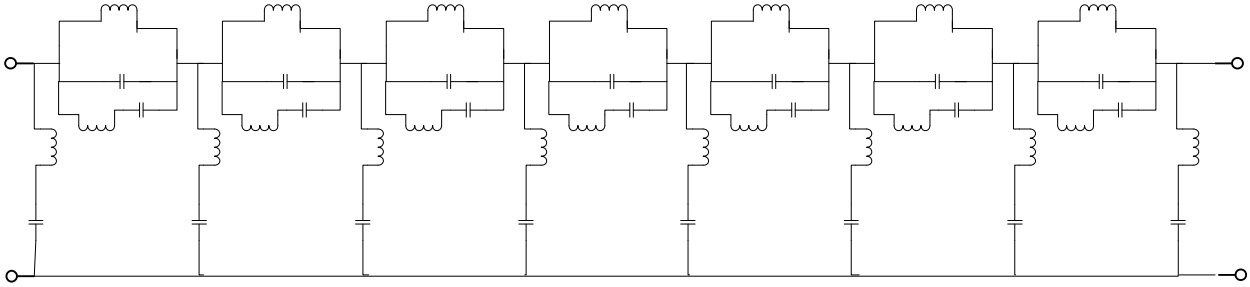

Figure 1-4 : Circuit Diagram for a 15th order elliptic function bandstop filter

As can be seen from the figure above, the doubly terminated bandstop filter topology is opposite to the bandpass one (shown in Figure 1-3); bandstop filters have series *LC* components in shunt branches, while bandpass filters have series *LC* components in series branches. The frequency response of this filter is shown below in Figure 1-5. The *LC* ladder filter response yields sharp skirt steepness due to the use of a high order elliptic function.

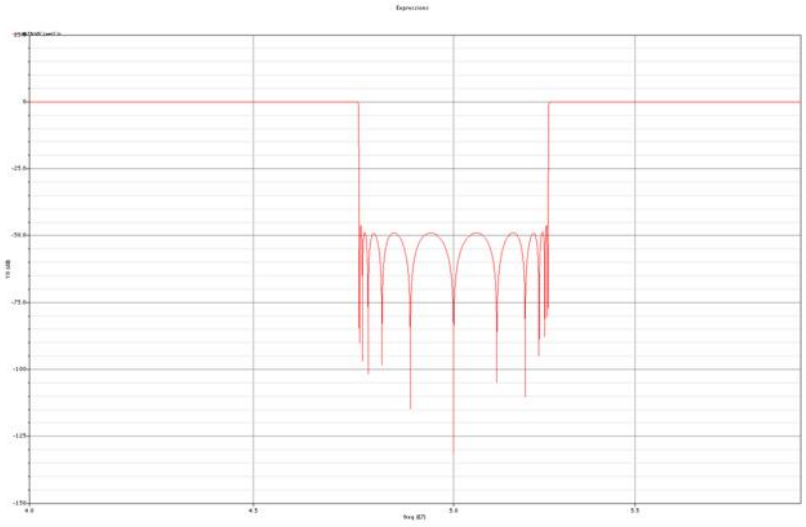

Figure 1-5 : Simulated frequency response of the bandstop *LC* ladder filter prototype

1.2.3 *LC* Lattice Filters

LC lattice filters were first introduced by Campbell in 1922 [8] and share many of the same attributes as *LC* ladders, such as low component sensitivities, and potential for high order performance. However, lattice filters are able to meet a wider range of filter requirements compared to ladder filters. For instance, allpass functions cannot be implemented using *LC* ladders because their transmission zeros lie on the imaginary axis [9].

Even though lattice structures are capable of realizing a wider array of filter functions, they have limitations that restrict their practicality. Lattice filters require higher terminating impedances and are more difficult to optimize, since all components interact with one another.

In this work, filter analysis and synthesis will be based only on ladder filter topologies.

1.3 Limitations to the Use of *LC* Passive Filter Design

LC passive filters have found widespread use, but there are limitations to their use and performance. *LC* filters only find applications in certain ranges of frequency. For instance, below audio frequencies, passive filter designs require high values of inductance and capacitance to realize the filter functions [1]. At these lower frequencies, common active filters and switched capacitor techniques are more practical because they can be designed to use smaller capacitance values. At very high frequencies, *LC* filters are limited by parasitic effects [9]. Practical inductor and capacitor values that satisfy these frequency limitations are given in Table 1-1.

Table 1-1 : Limitations of Inductor and Capacitor Values in Discrete Realizations. Adapted from [9]

Capacitors	
Readily realizable	5 pF-1 μF
Practical	0.5 pF-10 μF
Marginally practical	0.2 pF-500 μF
Inductors	
Readily realizable	1 μH-10 mH
Practical	0.1 μH-50 mH
Marginally practical	100 nH-1H

Passive *LC* filters also generally cost more and are bulkier to manufacture than active filters because of the high-quality coils required for the inductors in the design [1]. In addition, most *LC* filters require inductive element tuning to adjust the resonances present in the assembled circuit. In the case of a high order *LC* filter like the one shown in Figure 1-4, twenty-two inductor coils would need to be manually tuned. In addition, there is appreciable resistance in the coil windings which limit the filter *Q*'s.

1.4 Passive Filters Using Acoustic Wave Technology

This thesis explores the use of acoustic wave technology to address some of the limitations in passive *LC* filter networks. Acoustic wave devices are based on the use of piezoelectric materials. Piezoelectricity is a linear property in which polarization occurs when the material is subjected to mechanical stress. Inverse piezoelectricity refers to the appearance of mechanical stress upon application of an applied voltage. Early investigators in acoustic wave filter design acknowledged that higher performance passive electric filters could be realized by exploiting the coupling of electrical and mechanical fields in piezoelectric materials [10,11]. Earliest cases of such filters consisted of bulk acoustic wave (BAW) resonators, which are discussed in detail in Section 2.1.

Early studies demonstrated that acoustic wave filters have many advantages over *LC* filters. They offer potentially higher *Q*'s and are more compact than *LC* filters. They can be fabricated using IC techniques and can achieve filter responses across a much broader range of frequencies than *LC* filters.

Surface acoustic wave (SAW) filters provide a means for attaining low-loss, high performance bandpass filters in the VHF and UHF ranges [12]. As can be seen from Figure 1-6, SAW resonator filters attain reasonably high *Q*s in the hundreds of megahertz to gigahertz range while BAW filters are limited to frequencies below 100 MHz.

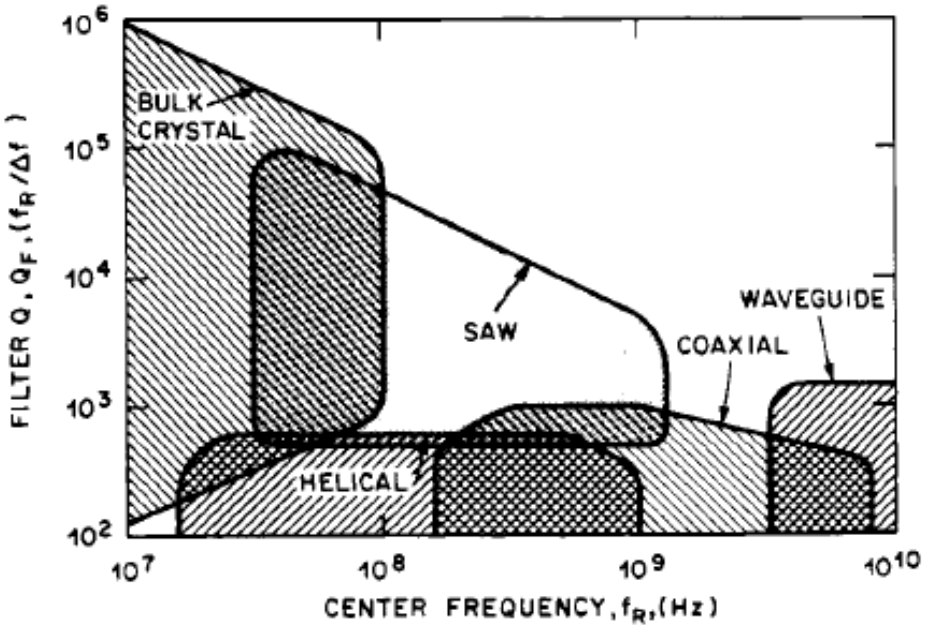

Figure 1-6 : Ranges of usability for various resonator filters. Reprinted with permission [12]

1.5 Thesis Aims

The goal of this thesis is to explore the use of surface acoustic wave devices to realize high-order passive filters. This is accomplished in two steps. In the first step the feasibility of building narrowband bandpass filters with commercially manufactured SAW resonators in a ladder network configuration is investigated. This also serves as a proof of concept for the use of SAW resonators in an impedance element filter topology. In the second step a method by which a SAW ladder filter can be optimized to most closely fit a standard *LC* filter response, such as Butterworth or Elliptic, is demonstrated.

The thesis is organized as follows. Chapter 2 includes a review of the theory of both bulk and surface acoustic wave devices. It concludes with expressions that relate the physical parameters of SAW resonators to the elements of an equivalent circuit

model. Chapter 3 describes methods of achieving bandpass filter responses with surface acoustic wave devices (both nonresonant and resonant). In addition, the theory of Impedance Element Filters (IEF) and their operation is presented in detail. Chapter 4 describes the fabrication and testing of a narrowband bandpass IEF network using commercial resonators. A method for designing a wideband SAW filter by optimizing the fit of its response to that of an elliptic filter approximation is discussed in Chapter 5. It is important to note that the term wideband is used somewhat loosely in this work. Instead of the formal definition of wideband, this work describes the filter presented in Chapter 5 as wideband in context of surface acoustic wave filter technology. Chapter 6 concludes the thesis and discusses future work.

2 Theory of Acoustic Wave Transducers and Resonators

2.1 Bulk Acoustic Wave Resonators

Early acoustic wave filters were composed of bulk acoustic wave resonators (BAW). In BAW resonators, metal electrodes are deposited on opposite faces of slabs of thickness *t* of a piezoelectric substrate (such as quartz, lithium niobate, etc…). A typical BAW resonator is shown in Figure 2-1, where the piezoelectric substrate is the area between the two metal electrodes. Figure 2-2 shows the equivalent circuit of a BAW transmitter, where C_T is the capacitance of the two electrodes of the BAW device and Z_m is the motional impedance of the resonator.

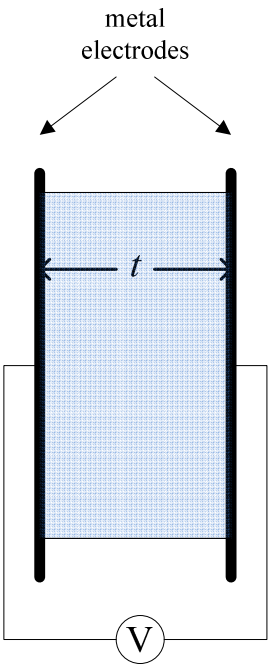

Figure 2-1 : Schematic of a BAW resonator. Adapted from [13]

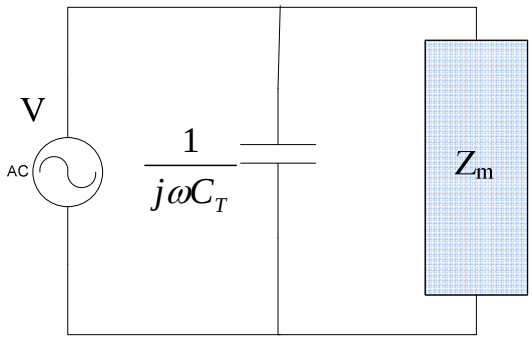

Figure 2-2 : Equivalent circuit for an acoustic wave transmitter. Adapted from [14]

In BAW resonators, acoustic waves are excited by the application of an electric potential at the same frequency and the waves propagate with a velocity, v_o, which is characteristic of the bulk substrate. Acoustic waves reflect from the boundaries of the slab, yielding a standing wave pattern which exists only for multiples of the resonant frequencies where the waves do not interfere destructively. These resonances are often referred to as Fabry-Perot modes. Figure 2-3 shows an example of such a condition, where the reactance of the motional impedance, Z_m, is plotted for a quartz BAW resonator.

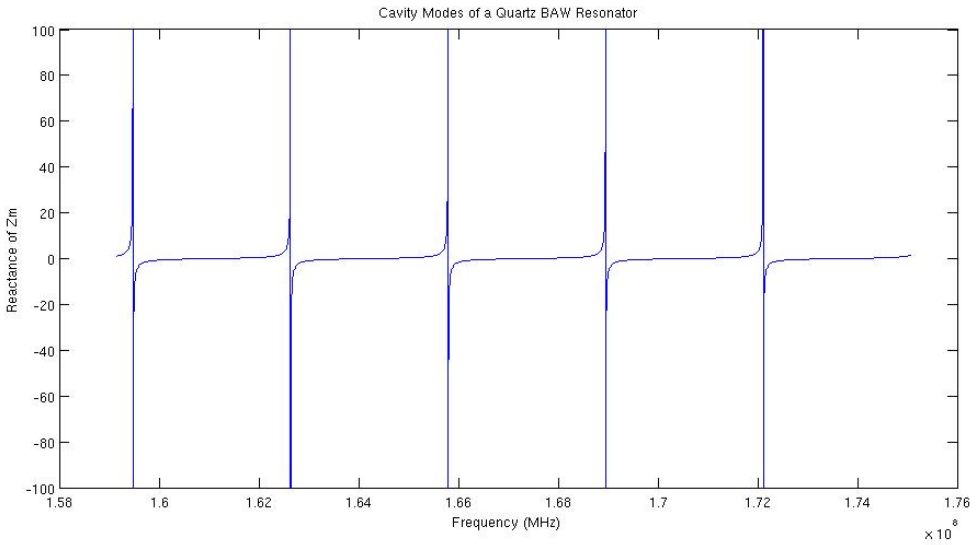

Figure 2-3 : Cavity modes of a quartz bulk acoustic wave resonator

The fundamental frequency of a BAW resonator occurs when the cavity thickness, *t*, is equal to half an acoustic wavelength, λ. The frequency and wavelength of an acoustic wave are related by the expression:

$$f = \frac{v_o}{\lambda} \tag{2-1}$$

so that frequencies of the cavity resonator, f_n, are given by:

$$f_n = n\frac{v_o}{2t} \equiv nf_{cav} \tag{2-2}$$

where n=1,2,3… Even multiples of f_n correspond to resonances of Z_m and odd multiples of f_n correspond to anti-resonances. At resonant frequencies, Z_m goes to zero and at anti-resonant frequencies, Z_m goes to infinity.

It can be shown that at frequencies near a resonant frequency, the BAW resonator behaves electrically as a Butterworth Van-Dyke (BVD) circuit [13]. It turns out that the

BVD model, shown in Figure 2-4, holds for both bulk and surface acoustic wave resonators.

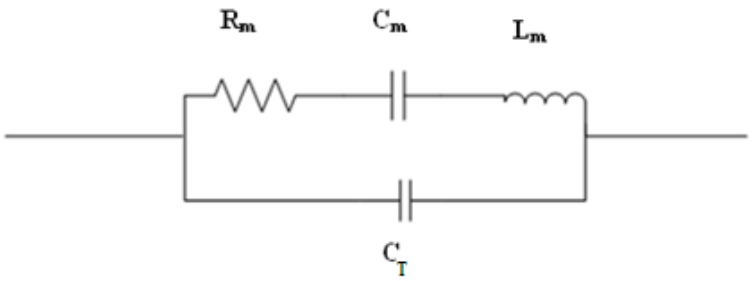

Figure 2-4 : Butterworth Van-Dyke equivalent circuit model for a BAW or SAW resonator

As shown in the figure above, series elements R_m, L_m, and C_m are referred to as the *motional* elements since they result from the interaction of electrical and acoustical fields. The shunt capacitance, C_T is due to the metal electrodes at each end of the piezoelectric slab. Figure 2-5 shows the typical magnitude and phase response for the impedance of a BAW resonator, using a BVD model.

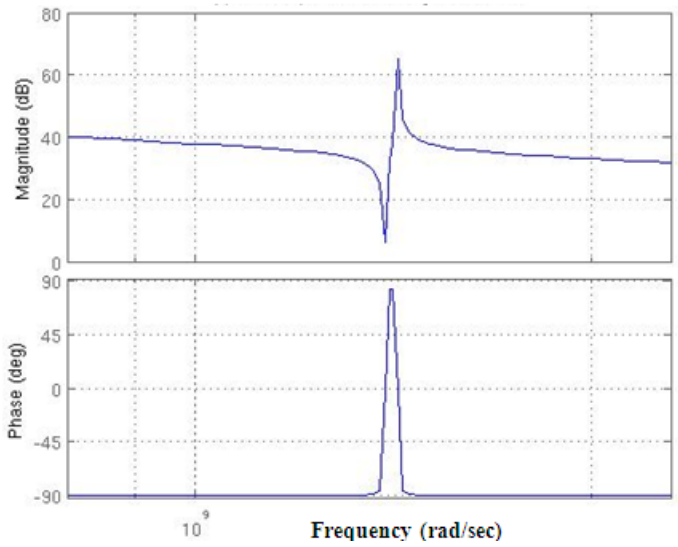

Figure 2-5 : Bode diagram of a typical BAW resonator using the BVD model

The series resonance of a BVD circuit is determined by the motional components of the resonator. At series resonance, the impedance is at its lowest value and the motional capacitance and inductance cancel. In contrast, the impedance goes to infinity at anti-resonance, a frequency higher than that of the series resonance, causing parallel resonance. In this case, no current leaves the circuit; it only recirculates about the circuit. Henceforth, the series resonance will be referred to as the resonance and the parallel resonance will be referred to as the anti-resonance of the BVD circuit.

The impedance of the Butterworth Van-Dyke circuit is:

$$Z_{BVD} = \frac{1}{sC_o} \frac{s^2 L_m C_m + sR_m C_m + 1}{s^2 L_m C_m + sR_m C_m + (1 + C_m / C_T)} \tag{2-3}$$

where $s=\sigma+j\omega$ is the complex frequency. Neglecting the motional resistance of the resonator, the frequencies of resonance and anti-resonance can be approximated as:

$$\omega_s \cong \sqrt{\frac{1}{L_m C_m}} \tag{2-4}$$

$$\omega_p \cong \sqrt{\frac{C_m + C_T}{L_m C_m C_T}} \cong \omega_s \sqrt{1 + \frac{C_m}{C_T}} \tag{2-5}$$

It has been shown that the relative difference between the anti-resonant and resonant frequencies is proportional to the electromechanical coupling coefficient, K^2, of the bulk piezoelectric material. This relationship is given by [13]:

$$\frac{\omega_p - \omega_s}{\omega_s} \approx \frac{4}{\pi^2} K^2 \tag{2-6}$$

The importance of the electromechanical coupling coefficient in acoustic wave devices will be discussed further in Section 2.4.

Another important parameter associated with the BAW resonator is the *Q*. As mentioned earlier in Equation (1-1), the resonator *Q* is equal to the ratio of the resonant frequency to the width of the resonance (see Figure 2-5). The *Q* of the resonator is given by:

$$Q = \frac{1}{\omega_s R_m C_m} \tag{2-7}$$

It is important to note that the motional resistance is the only part of the BVD circuit keeping the impedance from going to zero at resonance and to infinity at anti-resonance. Thus, when using high *Q* resonators which have very small motional resistances, the motional resistance can often be neglected in the design process.

Finally, as can be seen from Equation (2-2), the fundamental frequency, f_{cav}, of the BAW resonator is inversely proportional to the cavity thickness. Since the velocity of acoustic waves in most piezoelectric substrates is around 3000 m/s, BAW cavities with thicknesses of 1 µm – 10 µm result in fundamental frequencies of 100 MHz – 1 GHz. Since handling bulk crystals in this thickness range is difficult, BAW devices are not usually employed in VHF-UHF filter designs (see Figure 1-6).

2.2 Surface Acoustic Wave Resonators

In this section, the theory of operation of SAW transducers and resonators will be discussed and the relationship between physical resonator parameters and BVD circuit parameters will be presented. Before beginning the discussion, however, it is useful to review some basic background information on SAW propagation, devices, and resonators.

2.2.1 Surface Acoustic Wave Propagation

Surface acoustic waves are generated by the application of a voltage to an interdigital transducer placed on the surface of a piezoelectric solid. Electrical energy is then converted to mechanical energy in the form of surface acoustic waves via the piezoelectric effect.

A surface acoustic wave is a coupled vibrational/electrostatic wave confined to the surface of a piezoelectric substrate. The mechanical motion of a surface acoustic wave is depicted as a time-dependent displacement of the particles at the surface of the piezoelectric medium [15]. Generally speaking, this motion is shown in the figure below.

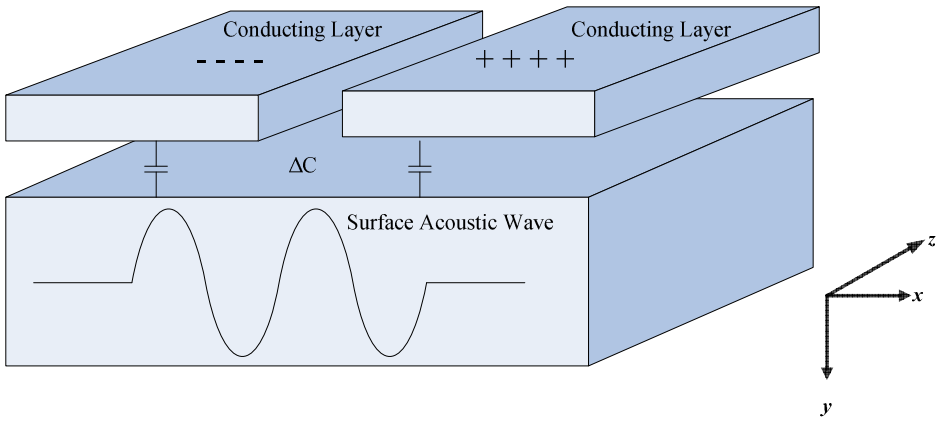

Figure 2-6 : Surface acoustic wave motion on the surface of an elastic structure. Adapted from [14]

As shown in Figure 2-6, Cartesian coordinates depict *x* as the axis of surface acoustic wave propagation and *y* as the surface normal axis. Surface particle motion is primarily in the *y*-*z*-plane, however not all crystal cuts exhibit this. In some cases, surface particles also move along the *x* axis.

The electrical potential at the surface of a piezoelectric substrate can be accurately represented as a travelling wave of potential such that

$$\varphi = \varphi_0(x,t) \cong \varphi_0 \exp\left[j(\omega t - \beta x)\right] \exp(-\beta |y|) \tag{2-8}$$

where φ is the electric potential in volts, ω is the angular frequency in radians per second, $\beta = 2\pi/\lambda$ is the propagation constant (sometimes referred to as k) in radians per meter, and λ is the acoustic wavelength of the surface acoustic wave. The term $e^{j(\omega t - \beta x)}$ represents the travelling wave propagating in the positive x-direction, while $e^{-\beta|y|}$ is the exponential decay factor which approximates the fall-off of the potential and field distributions away from the surface [14]. By virtue of the coupling between the electrostatic potential and

the mechanical motion, the mechanical displacement is also proportional to φ, with a different constant of proportionality for each component of the direction of motion and direction of propagation.

2.2.2 Surface Acoustic Wave Devices

Although the physical theories involved had been observed by Lord Rayleigh as early as 1855, applications of SAW technology to electronic devices wasn't investigated until 1965. The initial surface acoustic wave device in 1965 was the *interdigital transducer* (IDT) and it led the way for new approaches to analog filters, specifically in the range of 10 MHz to higher than 1 GHz. The research that evolved from these early discoveries spread rapidly and made its way into the consumer, commercial and military markets [15].

SAW-based devices and systems share many characteristics in common with BAW devices: high *Q* response characteristics, competitive pricing on high volume, relatively small component variation, and power efficiency [15]. The relationship between the acoustic wavelength, λ, and the SAW velocity, *v*, is:

$$\lambda = \frac{v}{f} \tag{2-9}$$

where *f* is the frequency of the SAW and *v* is the velocity of the SAW which is considerably different than the velocity of sound for bulk waves.

Figure 2-7 shows a basic SAW device consisting of an input IDT. The center wavelength, λ_o, of the acoustic wave packet generated by the input IDT is equal to twice the pitch, *p*, of the fingers:

$$\lambda_0 = 2p \tag{2-10}$$

since the mechanical strains introduced at each pair of fingers are added in phase for this wavelength [16]. An important consequence of (Equation 2-10) is that, photolithographic considerations usually limit the operational frequency range of SAW devices.

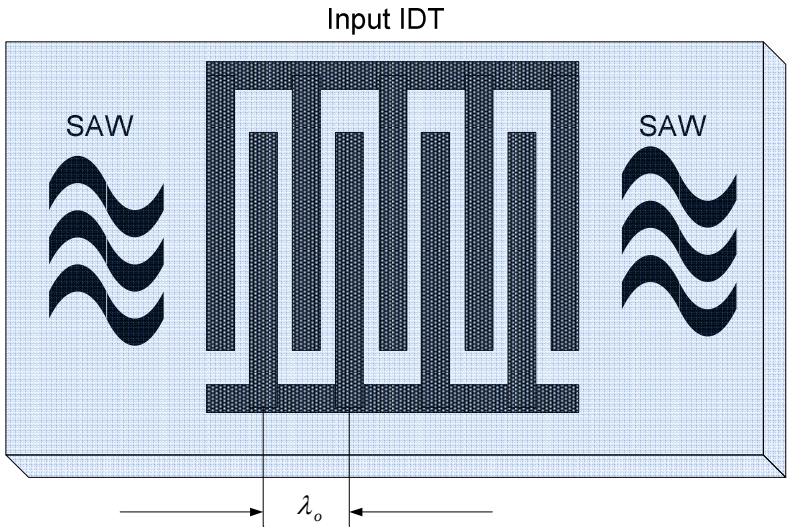

Figure 2-7 : Basic SAW device with thin-film input interdigital transducer. Adapted from [15]

Figure 2-8 shows the model for a SAW transmitter where $G_a(f)$ is the acoustic conductance of the device and $B_a(f)$ is the acoustic susceptance which is often ignored since it is very small for frequencies close to resonance.

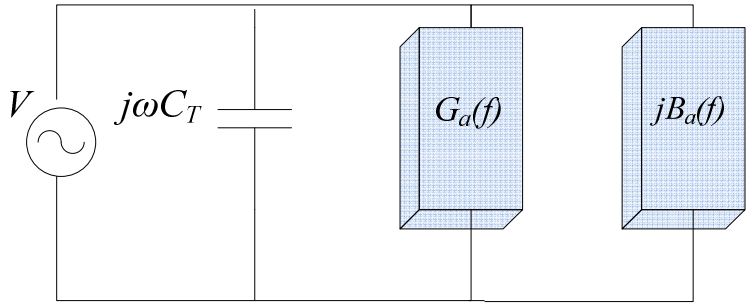

Figure 2-8 : Equivalent circuit for a SAW transmitter. Adapted from [14]

The frequency response of acoustic conductance in a SAW transducer has a sinc(X) dependence, where $X = \frac{N\pi(f - f_0)}{f_0}$. That is:

$$G_a(f) = G_{a0}\text{sinc}(X) \tag{2-11}$$

where G_{a0} is given by:

$$G_{ao} = \frac{2\,|aK^2|^2\,N^2 W y_0}{\lambda_0} \tag{2-12}$$

where a is a constant (a=0.8472 for η=0.5) that depends on the metallization ratio, η, representing the single-tap response function of the IDT, K^2 is the electromechanical coupling coefficient of $LiNbO_3$, and y_0 is the characteristic transmission line admittance of $LiNbO_3$. W is the overlap of the electrodes and N is the number of electrode pairs in the transducer.

A typical frequency response for $G_a(f)/G_{a0}$ is shown in the figure below.

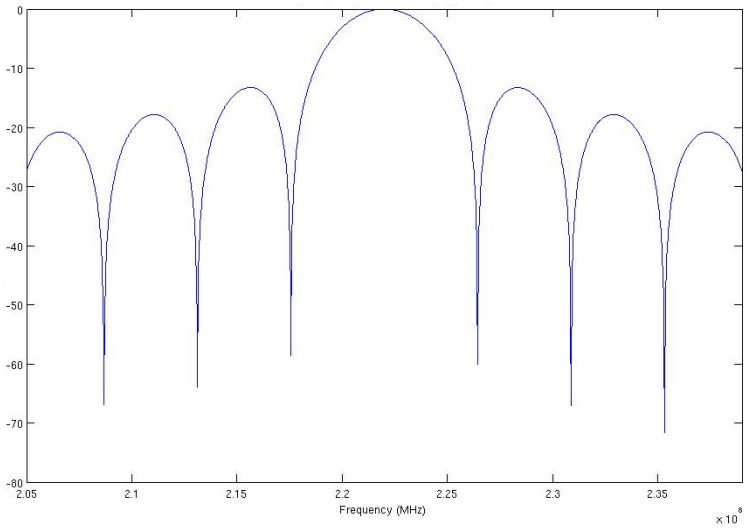

Figure 2-9 : Frequency response (normalized) of a 20log[$G_a(f)$] of a SAW transducer (in MHz).

The motional admittance of an individual SAW transmitter (seen in Figure 2-8) is equivalent to:

$$Y_{in} = j\omega C_T + G_a(f) + jB_a(f) \tag{2-13}$$

2.2.3 Surface Acoustic Wave Resonators

Surface acoustic wave resonators represent a class of SAW devices that includes individual surface acoustic wave transducers and mirrors that form resonant cavities. Just like the BAW resonator, these devices rely on *standing* surface acoustic waves, rather than *travelling* surface acoustic waves [15]. A SAW resonator can be constructed with a single interdigital transducer and two reflector gratings on either side. Incident and reflected waves within the SAW transmission line interfere with each other to form standing surface waves between the gratings. A diagram of a one-port resonator is shown in Figure 2-10.

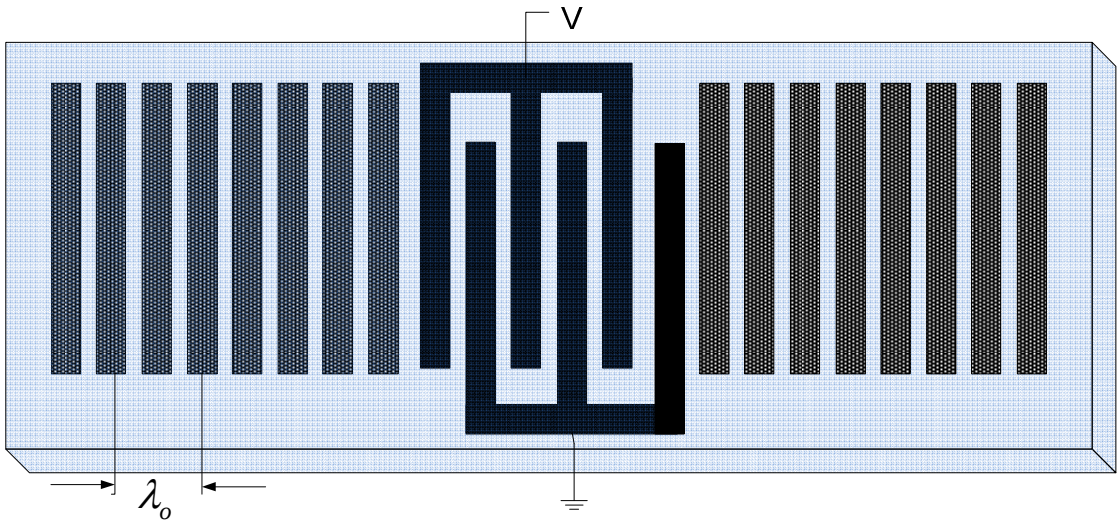

Figure 2-10 : Diagram of a one-port resonator. Adapted from [17]

As seen in the above figure, the gratings are placed on either side of the IDT and are normal to the direction of surface acoustic wave propagation. Reflector gratings can be formed by open or short-circuit strips of thin metal, or can be formed by etching thin pedestals into the substrate surface. The regular spacing of the gratings, or periodicity, is chosen so that at the transducer center wavelength, λ_o, SAWs incident on the grating are reflected backward. This type of reflection is known as the Bragg condition.

2.2.4 Theory of Surface Acoustic Wave Resonators

The Fabry-Perot model has been extensively used to describe the operation of SAW resonators. As shown in Figure 2-11, the total cavity length is equal to *L*, where $L = 2(L_p + d + {}^{N\lambda_0}\!/_2)$ as illustrated in the figure. The distance between the IDT and the mirrors is denoted as *d,* and L_p represents the effective length that surface waves

penetrate into the mirrors before being reflected back. It is important to note that this model ignores the effects of internal reflection within the transducer.

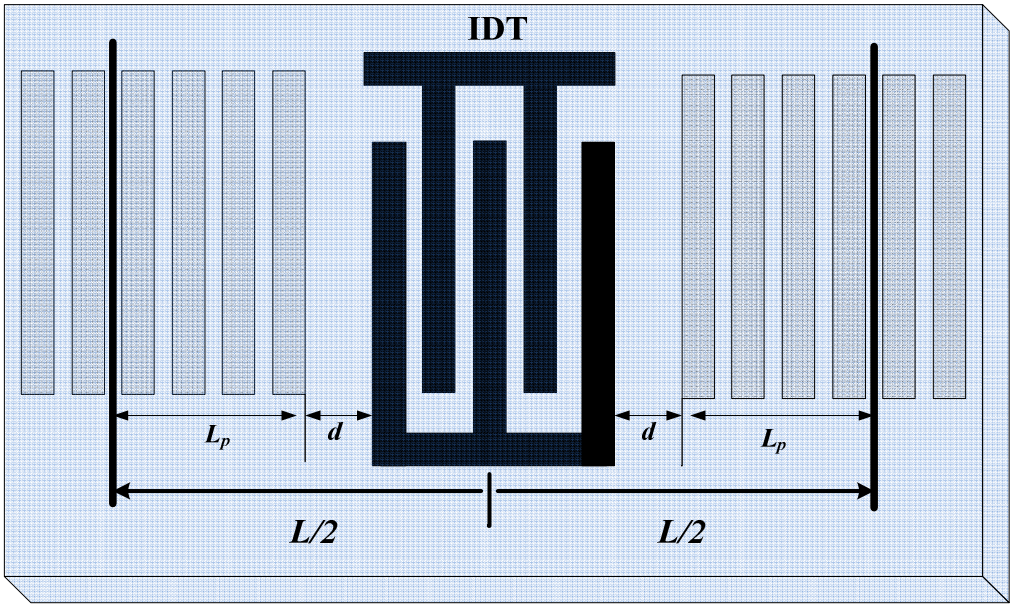

Figure 2-11 : Fabry-Perot model of a SAW resonator. Adapted from [18].

It has been shown by Datta [14] that the admittance of the transmitter (Equation (2-13)) changes greatly once the mirrors are included. It becomes:

$$Y_m \approx G_{a0} \frac{[1+|\Gamma_0|\exp(-2\beta Lj \pm \pi/2j)]^2}{1-|\Gamma_0|^2 \exp(-4\beta Lj \pm \pi)} \tag{2-14}$$

where $|\Gamma_0|=|\Gamma(f_0)|$ and $G_{a0}=G_a(f_0)$. $\Gamma(f)$ is the reflection coefficient of the mirrors and is dependent on the reflectance per electrode, r, and the number of electrodes in the mirror, N_m. As can be seen from Equation (2-14), resonances occur periodically when the denominator is equal to zero. These various resonant modes are commonly referred to as

longitudinal modes. The motional conductance for the SAW resonator is illustrated in Figure 2-12.

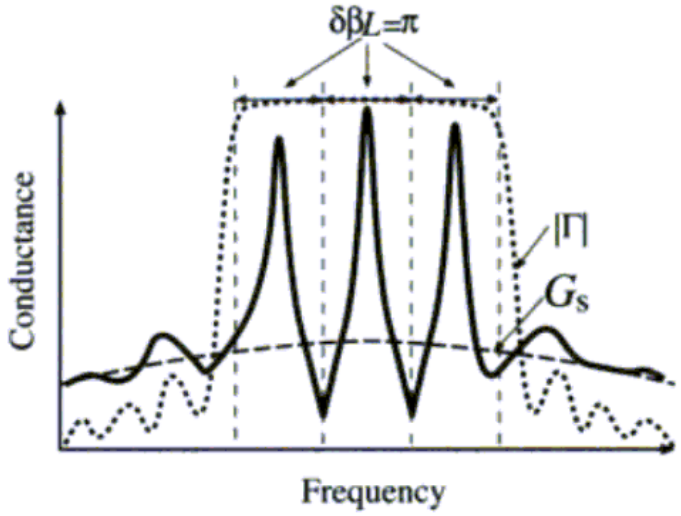

Figure 2-12 : Magnitude of motional conductance of a SAW resonator. Pending permission from [18]

As can be seen from this figure, the periodic resonances are entirely due to the mirrors.

The impedance of the motional components of a SAW resonator is given by:

$$Z_m \approx \frac{1}{G_a(f_o)} \frac{1-|\Gamma_0|^2 \exp(-4\beta L j \pm \pi j)}{\left[1+|\Gamma_0| \exp(-2\beta L j \pm \pi/2\, j)\right]^2} \tag{2-15}$$

It is assumed that the center frequency of the transducer, f_0 is equal to one of the cavity resonances.

Assuming that $f=f_0 \pm \Delta f$ and that $\Delta f << f_0$, the expression for motional impedance at frequencies near resonance becomes:

$$Z_m \approx \frac{1}{G_{a0}} \frac{(1-\left|\Gamma_0{}^2\right|) \pm \frac{j\Gamma 4\pi\Delta f L}{v_0}}{(1+\left|\Gamma_0{}^2\right|)} \tag{2-16}$$

It should be emphasized that this approximation for Z_m only includes the motional parts (*i.e.*, the series *RLC*) of the resonator. It does not include C_T.

The impedance of a series *RLC* circuit is given by:

$$Z_m' = R_m + j\left(2\pi f L_m - \frac{1}{2\pi f C_m}\right) \approx R_m \pm j4\pi\Delta f L_m \tag{2-17}$$

In this equation, R_m, C_m, and L_m denote the motional resistance, capacitance and inductance, respectively. Equating Equations (2-16) and (2-17), the equivalent circuit parameters are:

$$R_m = \frac{1}{G_{a0}} \frac{1-|\Gamma_0|}{1+|\Gamma_0|} \tag{2-18}$$

$$L_m \approx \frac{1}{4G_{a0} f_0} \frac{L}{\lambda_0} \tag{2-19}$$

$$C_m = \frac{1}{4\pi^2 f_o{}^2 L_m} \tag{2-20}$$

where $\left|\Gamma_0\right| = \tanh(N_m |r|)$ and G_{a0} is given by Equation (2-11) [13].

The approximation sign in Equation (2-19) arises from the assumption that $\Gamma \approx 1$ since the resonator is usually designed so that the magnitude of reflection coefficient of the mirrors is very close to unity at the center frequency. It is important to note that Equation (2-18) for R_m includes losses only due to imperfect mirrors and neglects losses

that occur due to viscous damping, diffraction of SAWs out of resonator cavity, etc… The additional losses add in series with R_m and diminish the overall Q of the cavity. Section 2.5 describes the overall Q of a cavity in greater depth.

Other than the motional parameters, the IDT capacitance, C_T, must be also be expressed in terms of resonator parameters. Such an expression is given by [14]:

$$C_T = N\sum_{\substack{odd \\ n}} 2C_n = NC_sW \tag{2-21}$$

where C_s is the sum of permittivities of the piezoelectric substrate and air (in pF/m).

2.3 Implications of the Fabry-Perot Model

It is important to emphasize implications associated with the assumption of the Fabry-Perot model. These implications can be shown from the expression for Z_m (Equation (2-15)), with Γ set equal to one:

$$Z_m = \frac{1}{G_a}\left(\frac{1-e^{(-2j\theta)}}{(e^{(-j\theta)}+1)^2}\right) = \frac{j}{G_a}\tan\left(\theta/2\right) \tag{2-22}$$

where $\theta = \frac{2\pi fL}{v_0}\,\mu\,\frac{\pi}{2}$. This equation shows that multiple anti-resonances (*i.e.*, Z_m goes to infinity) occur at:

$$f_{a,n} = f_0 \pm (2n+1)\frac{v_0}{2L} \tag{2-23}$$

and the resonances (when Z_m goes to zero) are at:

$$f_{r,n} = f_0 \pm n\frac{v_0}{L} \tag{2-24}$$

The resonances correspond to Fabry-Perot modes, which were seen before in the BAW resonator (see Equation (2-2)). It can be seen from Equations (2-23) and (2-24) that when the cavity length becomes large, cavity resonances and anti-resonances are very close together. Therefore, the theory developed above is only valid for frequencies close to f_0 where the next cavity anti-resonance is not excited. Thus, the expressions obtained for L_m and C_m are only applicable for frequencies very close to f_0. Recall that the anti-resonance of a BVD is given by:,

$$f_a = f_0\sqrt{1+C_m/C_T} \tag{2-25}$$

This means that f_a must be within $v_0/2L$ of f_0 in order to avoid the next cavity anti-resonance mode. Thus, the ratio of the motional and transducer capacitances must be extremely small. This constraint on the difference between resonance and anti-resonance frequencies also extends to BVD-based ladder networks and places a severe limit on the bandwidth that can be obtained with these networks.

Fortunately, recent work has shown that the limitations imposed by the assumption of the Fabry-Perot model can be partially overcome. As mentioned previously, the Fabry-Perot model is equivalent to the assumption that the reflections from electrodes in a transducer can be ignored. However, Hashimoto *et al.* [19] found that if these reflections are properly taken into account, the constraints placed by Fabry-Perot modes can be overcome in certain regions of the design space. Hashimoto showed that resonators in ladder-type SAW filters "use the internal reflection to suppress higher-order resonances."

2.4 Electromechanical Coupling Coefficient K^2

The electromechanical coupling coefficient K^2 (briefly mentioned in Section 2.2.4), relates the amount of power delivered to the load to the total stored energy in the structure [20].

The electromechanical coupling coefficient of bulk piezoelectric materials can be represented in terms of the piezoelectric coefficient e, stiffness constant c^E and dielectric constant (under static stress) ε^s:

$$K^2 = \frac{e^2}{c^E \varepsilon^s} \tag{2-26}$$

The electromechanical coupling coefficient for surface acoustic waves is:

$$K^2 = \frac{-\Delta W_E}{W_E} = \frac{2\Delta v}{v} \tag{2-27}$$

where W_E is the electrical energy stored in the transducer and $-\Delta W_E$ is the loss of electrical energy to acoustic energy over the length of the transducer (at the resonant frequency). Δv is the reduction in SAW velocity due to the surface electrodes, and v is the unperturbed SAW velocity. It can be shown that K^2 can also be expressed as [14]:

$$K^2 = \frac{2\pi C_s v_0}{y_0} \tag{2-28}$$

As previously mentioned in Section 2.1, the spacing of the resonant and anti-resonant frequencies of the BVD circuit for BAW resonators is proportional to the electrical coupling coefficient of a BAW resonator's substrate. This is also the case for

SAW resonators, where the ratio of the anti-resonant and resonant frequencies can be approximated by taking the first-order Taylor expansion of it:

$$\frac{f_a}{f_o} = \sqrt{1+\frac{C_m}{C_T}} \approx 1+\frac{1}{2}\frac{C_m}{C_T} \tag{2-29}$$

The ratio of the motional capacitance and the transducer capacitance can be found in terms of physical parameters using Equations (2-19) and (2-20):

$$\frac{C_m}{C_T} = \frac{2a^2K^4Ny_0}{\pi^2 f_0 LC_s} \tag{2-30}$$

Now using Equations (2-9) and (2-28), along with the assumption that for large values of N, $L/\lambda_0 \sim N$, the ratio becomes:

$$\frac{C_m}{C_T} = \frac{2a^2K^4Ny_0\lambda_0}{\pi^2 v_0 LC_s} = \frac{2a^2K^4Ny_0\lambda_0(2\pi C_s)}{\pi^2K^2Ly_0C_s} \cong \frac{4a^2K^2}{\pi} \tag{2-31}$$

The table below outlines electromechanical coupling coefficients and other important parameters for common piezoelectric substrates.

Table 2-1 : K^2 and other parameters for common SAW piezoelectric substrates. Adapted from [15]

Material	Crystal Cut	SAW Axis	Velocity (m/s)	K^2 (%)	Temp. Coefficient of Delay (ppm/˚C)
Quartz	ST	X	3158	0.11	0
$LiNbO_3$	Y	Z	3488	4.5	+94
$LiNbO_3$	128˚	X	3992	5.3	+75
$Bi_{12}GeO_{20}$	110	001	1681	1.4	+120
$LiTaO_3$	Y	Z	3230	0.72	+35

One major implication of the electromechanical coupling coefficient of a given piezoelectric substrate is its consequent bandwidth [20]. For instance, as shown in Table

2-1, Lithium Niobate, $LiNbO_3$, has a high coupling coefficient. Thus, lithium niobate is found in many wideband SAW filter applications. Conversely, ST-X quartz has a coupling coefficient which is almost 41 times less than that of $LiNbO_3$. This is why ST-X quartz lends itself easily to narrowband SAW filter applications. Figure 2-13 illustrates that using substrates with higher K^2 values allows larger bandwidths to be achieved. This graph shows the achievable resonator bandwidths assuming a center frequency of 222 MHz.

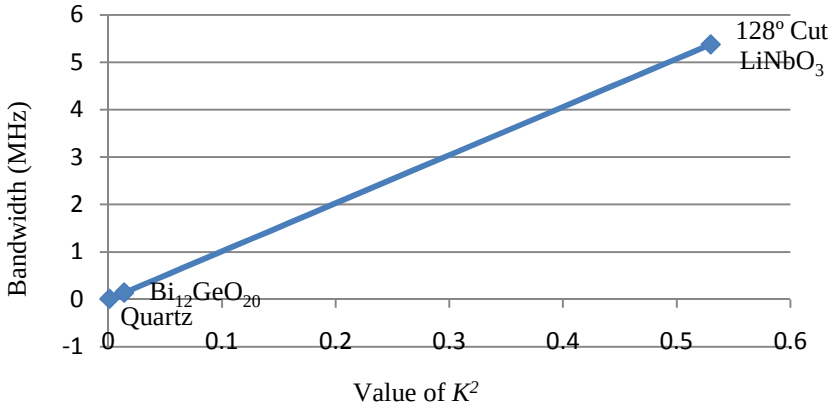

Figure 2-13 : Realizable resonator bandwidths for various coupling coefficients. This uses a center frequency of 222 MHz.

Less common piezoelectric substrates are also found in different applications. For instance, Lithium Tantalite, $LiTaO_3$, is also found in SAW oscillator designs, because of its lower temperature coefficient. In addition, bismuth germanium oxide ($Bi_{12}GeO_{20}$) is used in long delay line applications because of its relatively low surface acoustic wave velocity [15].

2.5 SAW Resonator *Q*

An important metric of any SAW resonator is its *Q*, or quality-factor. The total loaded *Q* of a resonator, or Q_L, can be represented as:

$$\frac{1}{Q_L} = \frac{1}{Q_m} + \frac{1}{Q_d} + \frac{1}{Q_r} + \frac{1}{Q_b} + \frac{1}{Q_c} + \frac{1}{Q_e} \tag{2-32}$$

Furthermore,

$$Q_L = \frac{f_0}{\Delta f} \tag{2-33}$$

Note that Equation (2-33) is equal to the reciprocal of the resonator fractional bandwidth. The various *Q* factors in Equation (2-32) are defined in Table 2-2.

Table 2-2 : Various *Q* factor definitions attributing to total loaded *Q*, Q_L of a SAW resonator. Adapted from [15]

Q	Type	Association
Q_m	Material *Q*	Viscous damping of the SAW on the substrate
Q_d	Diffraction *Q*	Losses because of diffraction in resonator and gratings
Q_r	Radiation *Q*	Losses of finite gratings
Q_b	Mode Conversion *Q*	Conversion to bulk waves
Q_c	External Coupling *Q*	Coupling external to the circuit
Q_e	Electrode *Q*	Finite resistance of metal film electrodes

2.6 Applications and Limitations of Surface Acoustic Wave Devices

There are many advantages of using SAW devices for filter applications. These include dependability, linear phase characteristics, reasonable temperature stability, and

relatively low cost. These devices can be used in a range of applications spanning from 10 MHz to 3 GHz. Aside from filters, surface acoustic wave devices have made their way into sensors, accelerometers, oscillators, pulse compressors, convolvers, correlators, multiplexers, and demultiplexers [16]. However, there are limitations in using these devices in these sorts of applications.

Limitations of the usability of SAW devices include special packaging and expensive fabrication processes. Particular packaging is required because of how easily the surface acoustic waves can be disturbed by change at the surface of the substrate. Also, the type of packaging used greatly impacts the insertion loss of the device. Another limitation of surface acoustic wave devices is the necessary fabrication processes and materials involved. The fabrication can become very expensive, especially when using substrates other than quartz.

3 Methods of Achieving Bandpass Filter Responses with SAW Devices

3.1 Bandpass Filtering Using Surface Acoustic Wave Devices

This section will explore several SAW structures that can achieve a bandpass filter function. Generally speaking, SAW filters can be constructed using either nonresonant or resonant structures. That is, resonant filter structures use reflective gratings on either side of the transducers whereas nonresonant filter structures do not. Both formations will be described in this section, with special attention paid to the former since these are the basis of the filter designs discussed in this work.

3.1.1 Low-Loss Non-resonant Filters

This section serves as a brief overview of low-loss filter structures that utilize non-resonant SAW devices. Although not inclusive of all methods and topologies presently used in low-loss non-resonant networks, this section does serve to illustrate the advantages and disadvantages of this class of SAW filters.

3.1.1.1 Interdigitated Interdigital Transducer (IIDT) Filter

Interdigitated Interdigital Transducer (IIDT) filters emerged from the needs of modern communication systems in the range of 1-2 GHz. Although IIDT filters can exhibit low insertion loss (< 6dB), it is difficult to fabricate IIDTs with good stopband attenuation [21]. The diagram of the basic IIDT filter can be seen in Figure 3-1. As can be seen, the IIDT is composed of several cascaded IDTs which are connected alternately to the input and output.

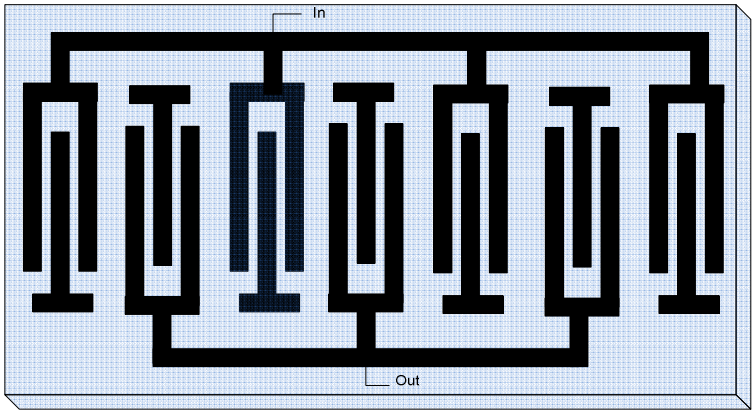

Figure 3-1 : Diagram of an IIDT, a type of low-loss non-resonant filter.

Two main advantages of IIDTs in filtering are 1) their power handling ability (due to wide transducer area), and 2) their small electrode resistance. The total electrode resistance is small because the electrodes are connected in parallel [22]. In IIDT filters, insertion loss is not significantly affected by the electrode resistance.

Although modifications can be made to the basic IIDT structure that increase stopband attenuation and reduce insertion loss, this structure still exhibits many undesirable characteristics. Because IIDT filters can be internally impedance-matched at only one frequency, passband ripple can be very poor. Also, networks that incorporate IIDTs require careful design to avoid interference by adjacent IDTs that may result in degradation of IIDT insertion loss [23].

3.1.1.2 Transversal Filters with Apodized Transducers

Transversal bandpass filters using apodized transducers offer good performance and are very reproducible. Apodization is the variation in individual electrode lengths in SAW interdigital transducers. A typical apodized SAW device usually involves one

apodized and one unapodized transducer [23]. Figure 3-2 shows a diagram of a basic bandpass filter using an apodized transducer. This bandpass filter design was first reported by Hartemann and Dieulesaint in 1969 [24].

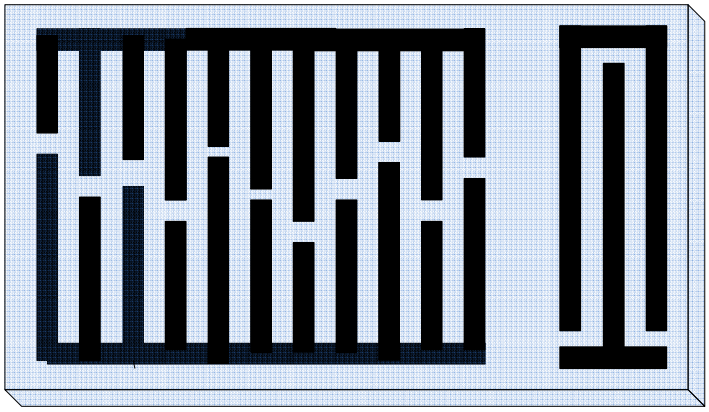

Figure 3-2 : Bandpass filter using an apodized transducer. Adapted from [24]

Apodization is a versatile technique in that it offers the possibility of realizing an FIR approximation for virtually any desired frequency response. In the case of an apodized transducer, the charge distribution is directly proportional to the finger overlap. As a consequence, it can be shown that a good approximation to the desired frequency response can be obtained by matching the electrode overlap to the inverse Fourier transform of the desired response function. Despite the advantages of transversal filters with apodized transducers, there are a few limitations. In designing of filters in this class it is necessary to compensate for second-order effects like distortion associated with the terminating impedances [23]. In addition, these filters generally exhibit very poor insertion loss [23].

3.1.2 Low-Loss Resonator Filters

In this section two low-loss resonator filters are described. Once again, this section is not inclusive of all methodologies currently used for resonant filter structures.

3.1.2.1 Transverse-Coupled Resonator Filters (TCRFS)

Transverse-Coupled Resonator Filters (TCRFs) are often used in narrowband filters and exhibit low insertion loss across the passband and a high stopband rejection. Although they are most widely used in bulk-wave crystal resonators, methods have been invented to extend their application to quartz SAW resonators. This is accomplished by acoustically coupling all resonators in the filter [23]. Figure 3-3 shows the schematic layout of a transverse-coupled resonator filter.

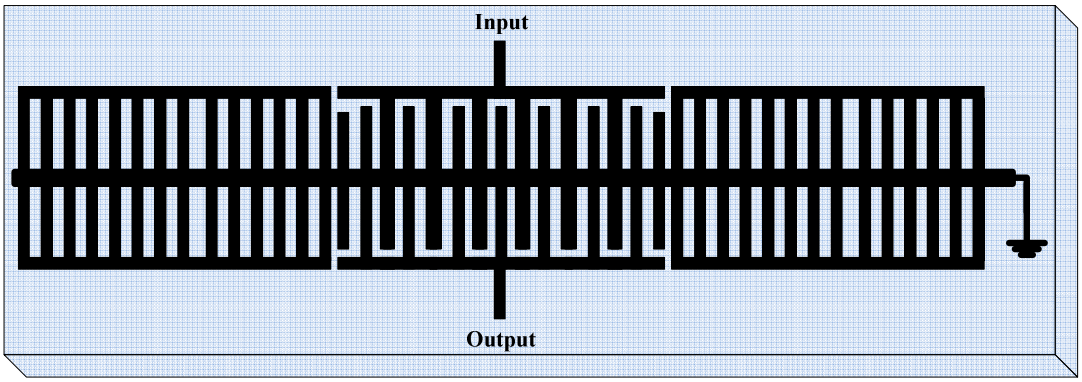

Figure 3-3 : Transverse-coupled resonator filter. Adapted from [25]

As can be seen from Figure 3-4, a TCRF consists of two identical tracks, which can be seen as a one port resonator. For this specific type of filter, only the fundamental and first symmetric modes are of importance. Assuming a TCRF is matched to the generator and load impedances, a narrowband response with little ripple is obtained. To improve on the steepness of passband skirts and the stopband rejection, this structure can be cascaded

[25]. Cascades of two TCRFs have been fabricated to realize high performance narrowband filters with insertion losses of less than 5 dB and stopband attenuations greater than 40 dB [25].

Although the performance of a TCRF is quite competitive, there are still drawbacks and limitations with this structure. First of all, these filters lend themselves primarily to narrowband applications. TCRFs fabricated on quartz exhibit very narrow bandwidths of approximately 700 ppm [25]. Another drawback of this type is the coupling that can occur between tracks in the device and cause excitations of unwanted modes.

3.2 Impedance Element Filters (IEF)

3.2.1 Bandpass Filter Design using Six Element IEF Structure

For VHF-UHF applications, the Impedance Element Filter (IEF) structure has many advantages. Unlike SAW filter structures like those described in Section 3.1, IEFs can be designed to exhibit flat passbands with little insertion loss. Their stopband attenuation is reasonable and second-order effects are not an issue. Figure 3-4 shows a six element IEF ladder. This configuration is used for both the wideband and narrowband filter designs presented later in this chapter.

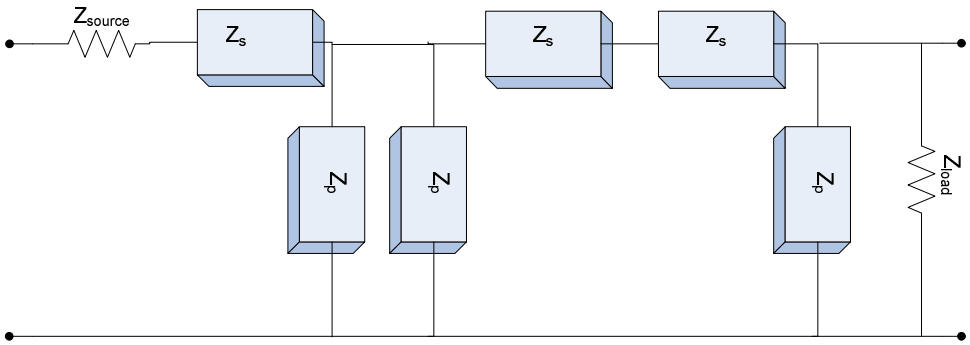

Figure 3-4 : Circuit schematic of six element IEF structure; each block represents a BVD equivalent of the associated SAW resonator

This figure can also be simplified for analysis and represented as the network shown in Figure 3-5. Specifically, this is accomplished by assuming all series impedances are equal and all parallel impedances are equal.

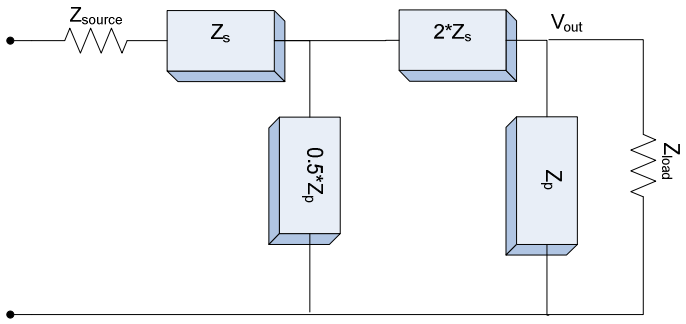

Figure 3-5 : Circuit schematic of six element IEF structure, simplified for analysis

The most important requirement of this design is that the anti-resonant frequencies of the parallel resonators should approximately equal the resonant frequencies of the series resonators:

$$\omega_{ap} = \omega_{rs} \tag{3-1}$$

A widely accepted representation of a filter's performance is its s-parameter transmission, S_{21} (see Appendix Section 7.2).

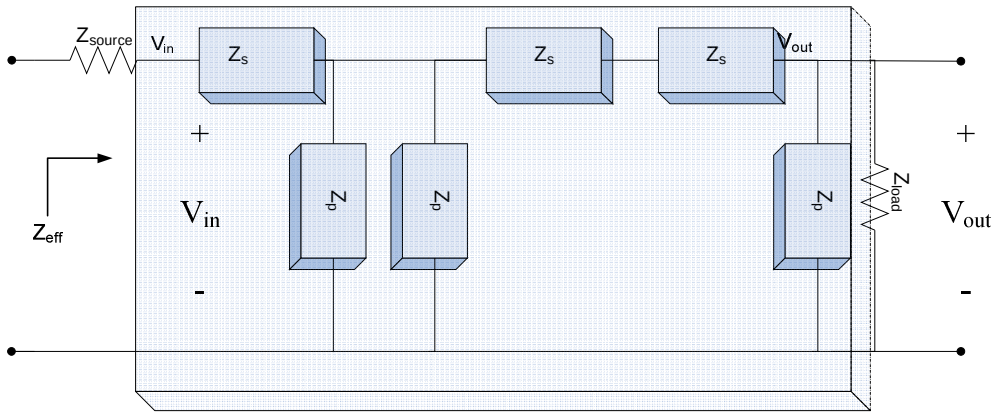

Figure 3-6 : Two-port network representation of six element IEF bandpass design

Referring to Figure 3-6, the ratio V_{out}/V_{in} represents the voltage transfer function of the network. The S_{21} of the network representation shown in the figure above is:

$$S_{21} = \frac{V_{out}}{V_{in}}(1+\rho) \tag{3-2}$$

where rho (ρ) represents the reflection coefficient of the filter network, or the S_{11} which is given by:

$$S_{11} = \frac{Z_{eff} - Z_{load}}{Z_{eff} + Z_{load}} \tag{3-3}$$

Z_{eff} is the impedance looking into the network, shown in the box in the figure. This impedance is equal to:

$$Z_{eff} = \left\langle \left\{ \left(\left[(Z_{load} \parallel Z_p) + 2Z_s \right] \parallel Z_p \right) \parallel Z_p \right\} + 2Z_s \right\rangle \tag{3-4}$$

The transfer function of the filter network, $T_6(s)$, can be represented as:

$$T_6(s) = \frac{V_{out}}{V_{in}} = \frac{Z_{load}}{\frac{4Z_s^{\,2}Z_{load}}{Z_p^{\,2}} + \frac{4Z_s^{\,2}}{Z_p} + 3Z_s + \frac{5Z_{load}Z_s}{Z_p} + Z_{load}} \tag{3-5}$$

where $s = \sigma + j\omega$ is complex frequency. From this equation it can be seen that at the resonant frequency of the parallel resonator ($Z_p(\omega_{rp})=0$), the transfer function, $T_6(s)$, is equal to zero. Moreover, at the resonant frequency of the series resonator ($Z_s(\omega_{rs})=0$), the transfer function is equal to one. Thus, the parallel resonant frequency represents the leading edge of the stopband and the resonant frequency of the series impedance indicates a point in the passband. Moreover, the anti-resonant frequency of the series impedance ($Z_s(\omega_{as})=\infty$) represents the trailing edge of the passband. This is illustrated by Figure 3-7, which shows a typical bandpass response of an IEF, with the parallel and series impedances superimposed.

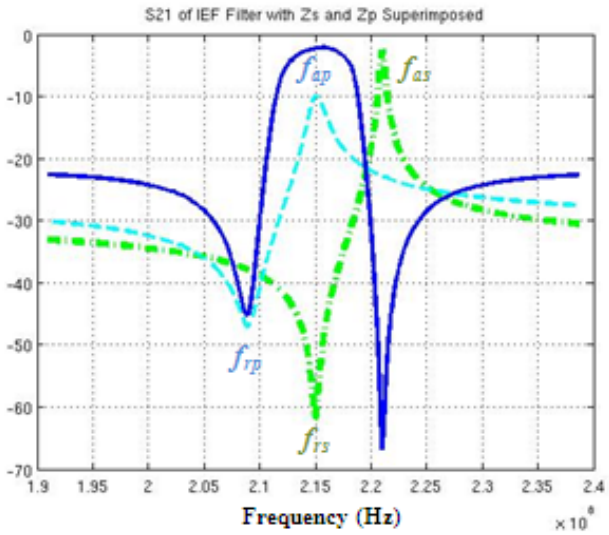

Figure 3-7 : Responses as a function of frequency: a) 20log(|S_{21}|) of a typical IEF bandpass filter (solid blue), b) 20log(|Zs|) (dash-dotted green), and c) 20log(|Zp|) (dashed cyan) (Note all plots are not to the same scale. The scale at the left refers only to the IEF bandpass response)

As this figure shows, the minima of the bandpass response occur at the resonant frequency of the parallel impedance and the anti-resonant frequency of the series impedance.

3.2.2 Impedance Matching in an IEF Structure

The general IEF structure shown in Figure 3-4 is known to be of "constant-*k*" form [26]. It can be shown that a critical condition for impedance matching is [5]:

$$Z_s \times Z_p = R^2 \tag{3-6}$$

where Z_s and Z_p are the impedances of an individual stage of the IEF structure (see Figure 3-8) and R is the transmission line impedance.

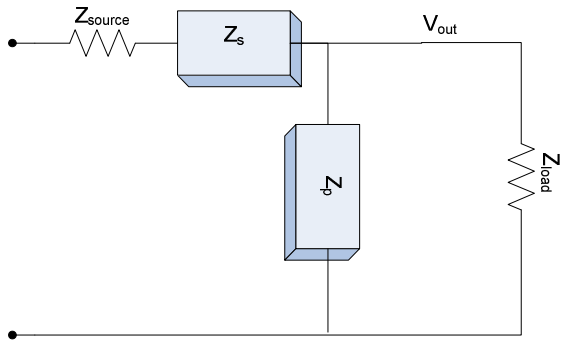

Figure 3-8 : Single stage of six element IEF structure

Equation 3-6 imposes constraints on the circuit elements that comprise Z_s and $Z_{p.}$ In order to derive these constraints, the following assumptions are made for each stage of the filter [26]:

$$\omega_{ap} \cong \omega_{rs,}$$

$$\omega_o - \omega_{rp} = \omega_{as} - \omega_o$$

$$\omega_o = \frac{\omega_{as} + \omega_{rp}}{2},$$

$$\Delta\omega_o = \frac{\omega_{as} - \omega_{rp}}{2},$$

$$2\omega_o >> \Delta\omega_o \tag{3-7}$$

Evaluating Equation 3-6 at the center frequency, ω_o, and using the first and second equations in (3-7) the product of the series and parallel impedances is:

$$Z_s \times Z_p = \frac{(\omega_o{}^2 - \omega_{rp}{}^2)}{-\omega_o{}^2 C_{Ts} C_{Tp} (\omega_o{}^2 - \omega_{as}{}^2)} = \frac{(\omega_o + \omega_{rp})}{\omega_o{}^2 C_{Ts} C_{Tp} (\omega_o + \omega_{as})} = R^2 \tag{3-8}$$

Substituting the third and fourth equations into (3-7) into (3-8) yields:

$$Z_s \times Z_p = \frac{(2\omega_o + \Delta\omega_o)}{\omega_o{}^2 C_{Ts} C_{Tp} (2\omega_o - \Delta\omega_o)} = R^2 \tag{3-9}$$

Now, taking the last equation in (3-7) into account, Equation 3-9 becomes [26]:

$$Z_s \times Z_p = \frac{1}{\omega_o{}^2 C_{Ts} C_{Tp}} = R^2 \tag{3-10}$$

Equation 3-10 shows that internal impedance matching in IEF designs can be achieved by adjusting the values of shunt capacitances in the resonators. Satisfying this relationship is advantageous since it eliminates the need for an external matching network.

4 Proof of Concept: Realizing Bandpass Filters with Commercial Quartz SAW Resonators

A narrowband bandpass filter was designed using the Impedance Element Filter topology described in Section 3.2. This section discusses the performance of a bandpass filter based on commercial one-port quartz SAW resonators in an IEF configuration.

4.1 Narrow Bandwidth Filter Design

4.1.1 Design Constraints

Since the narrowband bandpass filter design utilizes commercial SAW quartz resonators, there are many constraints to the design. Commercially available resonators purchased at low costs and in low volumes are limited with respect to center frequency selection, substrate type, and packaging. As shown in Table 4-1, four of the primary SAW resonator manufacturers are included in this table: Golledge, EPCOS, Murata and RF Monolithics, Inc. As can be seen in Table 4-1, one-port commercial SAW resonators are primarily fabricated on quartz substrates. As discussed in Section 2.4, bandpass filter designs using commercial resonators will necessarily have a narrow passband due to the low electromechanical coupling coefficient of quartz (see Table 2-1).

Table 4-1 : Comparison of Commercially Available One-Port Surface Acoustic Wave Resonators for Low Cost and Low Volume Applications

Manufacturer	Material	Frequency Range	Available Packaging
Golledge	Quartz	110 MHz – 1.1 GHz	4, 6, 8, 10, 12 Pin SMD F-11 and TO-39 TH
EPCOS	Quartz	315 MHz – 915 MHz	4, 6 Pin SMD
Murata	Quartz	304 MHz – 434 MHz	6 Pin SMD
RF Monolithics, Inc.	Quartz	293 MHz – 980 MHz	2, 4, 6, 8 Pin SMD TO-39 TH

The narrowband design is also limited by the restrictions related to accuracy and usability of the design. For example, special attention needs to be paid to tolerance issues of the resonators. Commercial SAW resonators have resonant frequencies within 50 kHz-100 kHz of their nominal values. Better performing bandpass IEFs can be designed if the exact resonant and anti-resonant frequencies are known for each resonator before implementing them in an IEF topology. This is because the anti-resonant frequency and the resonant frequency of the parallel and series resonators must be very close in value (as described in 3.2.1).

4.1.2 Design of the Characterization Board

The characterization board was used to characterize a broad array of individual resonators in order to find the closest matched commercial resonators. For simple testing, through-hole resonators in TO-39 packages were chosen. That way, TO-39 transistor

sockets could be used and the resonators could be easily switched on and off the board. These resonators are shown in Figure 4-1.

Figure 4-1 : Picture of commercial SAW resonator in a TO-39 package. Copied from [27]

The prototype board designed for characterization includes one three-pin TO-39 transistor socket, where two pins accept each port of a SAW resonator and the last pin serves as a case ground. This PCB includes two small traces to the center conductors of edge mount SMA connectors. The PCB footprint for the characterization board is shown in Figure 4-2.

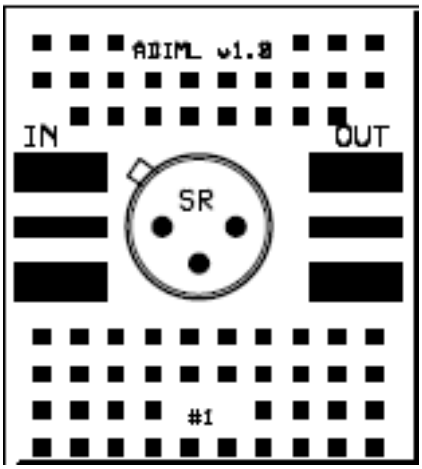

Figure 4-2 : Footprint for PCB used for characterization of commercial SAW resonators

As can be seen from the above figure, this PCB was built to accommodate only one resonator at a time. An image of a single, populated characterization board is seen in Figure 4-3.

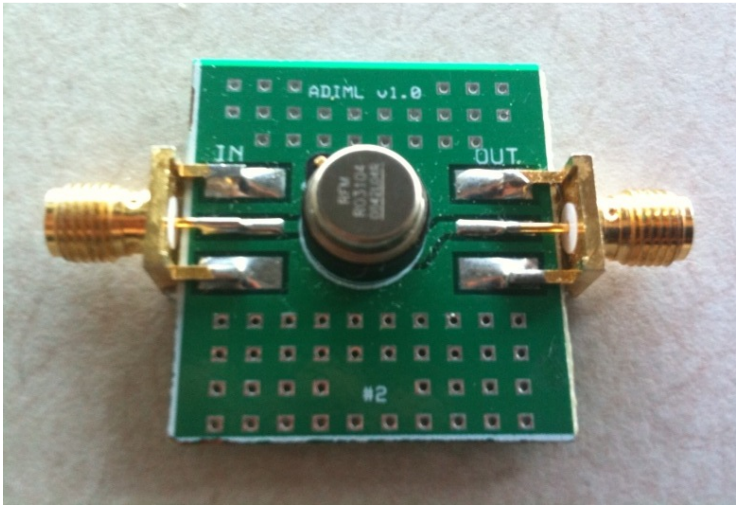

Figure 4-3 : Image of a single, populated characterization board

Measuring each resonator separately not only helped match resonators in series and parallel branches of the IEF ladder, but it also ensured accurate parameter extraction. Using the characterization board, the S_{21} of each resonator was measured as a function of frequency using a two-port network analyzer. The maximum and minimum S_{21} attenuations (in dB) and the frequencies at which they occurred were recorded for each resonator. With these four measurements, the equivalent BVD parameters could be extracted[1].

[1] Section 7.2 of the Appendix includes a detailed explanation of parameter extraction and Section 7.3 includes the MATLAB code used for it.

4.1.3 Design of Narrowband Filter

A narrowband filter prototype board was designed and built to accommodate six commercial SAW resonators in TO-39 packages. Several steps were taken to minimize parasitic effects including ground stitching, isolating traces, and having gradual trace corners. These are shown in Figure 4-4.

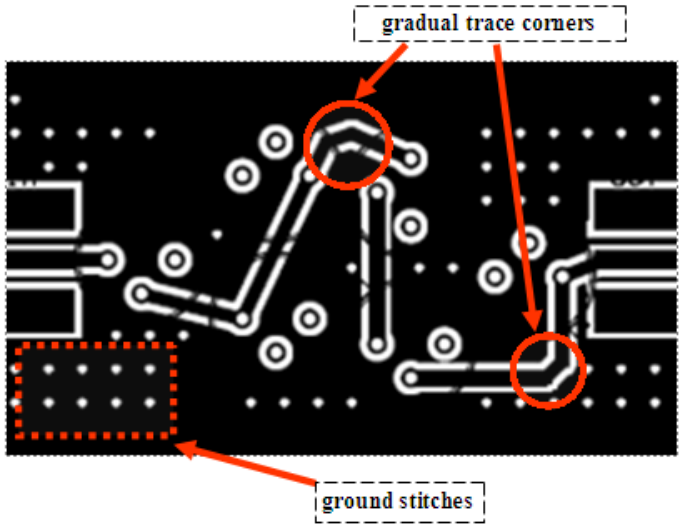

Figure 4-4 : Efforts taken to minimize parasitic effects in narrowband design

The narrowband filter prototype board is quite similar to the characterization board in that both are configured to use SMA connectors, and both fit TO-39 transistor sockets. The best-fit resonators identified in the characterization phase were installed on the narrowband filter PCB. Figure 4-5 shows the schematic of the PCB designed for the narrowband commercial SAW resonator filter. Part numbers are also included in this schematic.

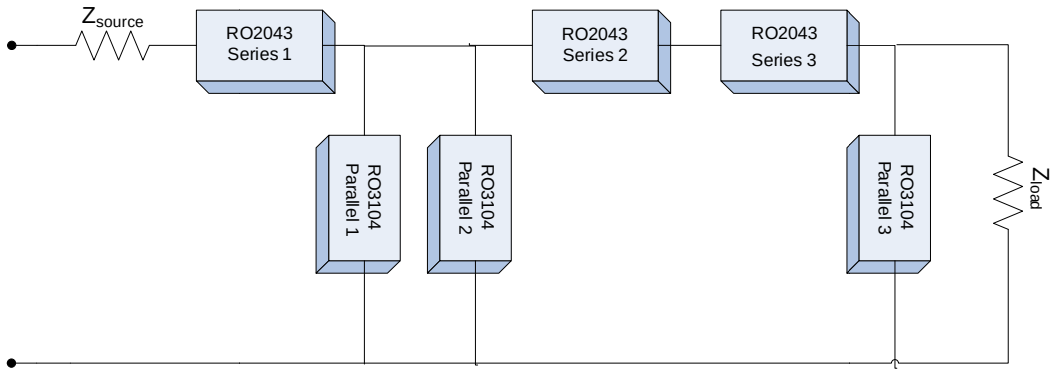

Figure 4-5 : Schematic for narrowband filter PCB design using commercial SAW resonators

The PCB related to this schematic is shown in Figure 4-6 and shows only the top silkscreen layer, pads, and text on the board.

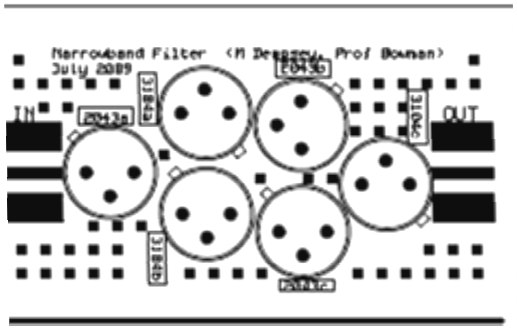

Figure 4-6 : Layout of narrowband filter PCB designed to use commercial resonators. Figure shows silkscreen, pads, and text

The top copper layer is shown below in Figure 4-7.

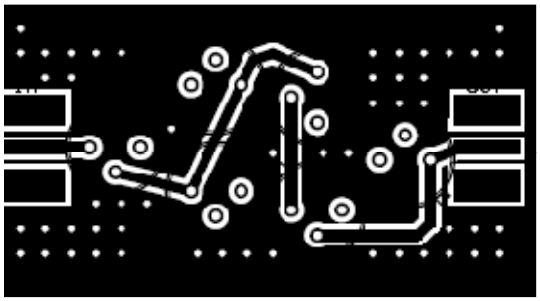

Figure 4-7 : Layout of narrowband PCB design, showing top copper layer

Last of all, Figure 4-8 shows the image of a single populated narrowband filter prototype board.

Figure 4-8 : Image of a single, populated narrowband bandpass filter board

The narrowband filter was optimized by finding three closely matched RO3104 resonators with resonant frequencies slightly above their nominal value. The anti-

resonant frequencies of these devices were computed and then the three most closely matched RO2043 resonators were selected.

4.2 Measurement Results

Measurements on the individual SAW resonators and on the narrowband filter shown in Figure 4-3 and Figure 4-8, respectively, were carried out using an Agilent Technologies Model E5071C two-port network analyzer. The network analyzer used precision adapters and was calibrated using a 7/16 Calibration Kit.

4.2.1 Individual SAW Resonators

As discussed in the Section 4.1, two sets of three closely matched resonators were chosen for the parallel and series branches of the narrowband IEF ladder network design. Table 4-2 shows the anti resonant and resonant frequencies of the six resonators chosen.

Table 4-2: Resonant and anti resonant frequencies of the six commercial SAW resonators chosen for the narrowband design.

Resonator	f_r (MHz)	f_a (MHz)
RO2043a	303.8817	303.9477
RO2043b	303.8240	303.8937
RO2043c	303.8577	303.9237
RO3104a	303.7579	303.8913
RO3104b	303.7567	303.8901
RO3104c	303.7580	303.8949

Despite the variation in commercial resonators it was possible to match the two sets of resonators quite closely. The parallel-branch resonators all ended up having anti-resonant frequencies around 303.89 MHz.

Parameter extraction was performed using the characterization board described in 4.1.2 and methods described in the Appendix. The equivalent BVD circuit parameters are listed in the table below.

Table 4-3 : Equivalent BVD circuit parameters for the six resonators used in the narrowband filter design (see Appendix for description of parameter process)

Resonator	Motional Resistance, R_m (Ω)	Motional Inductance, L_m (μH)	Motional Capacitance, C_m (fF)	Shunt Capacitance, C_T (pF)
RO2043a	74.1444	414.7612	0.6613525	1.5224
RO2043b	80.1839	374.8495	0.7320474	1.5953
RO2043c	72.3572	413.7564	0.6630634	1.5262
RO3104a	28.4374	169.8457	1.6163	1.8408
RO3104b	29.0323	165.4531	1.6593	1.8896
RO3104c	22.9095	145.0287	1.8929	2.0990

As seen in Table 4-3, the equivalent circuit parameters have a wide range of values for each set of resonators. The motional inductances and capacitances vary in value, which results in slightly different resonant frequencies. Moreover, the motional resistances exhibit an even broader range of values. Larger motional resistances indicate that the resonators will have greater insertion loss. As discussed in Section 2.2.2, the ratio of the motional to the shunt capacitances directly impacts the anti-resonant frequency. Recall that the difference between the anti-resonant frequency and the resonant frequency is directly proportional to this ratio.

The spectral impedance response for single resonators was measured and was simulated both in MATLAB and in Cadence using the equivalent circuit parameters shown in Table 4-3. Figure 4-9 compares results of measurement and simulation. Measured results are in shown in black and simulation results are in gray. As can be seen, the agreement between simulation and measurement is good.

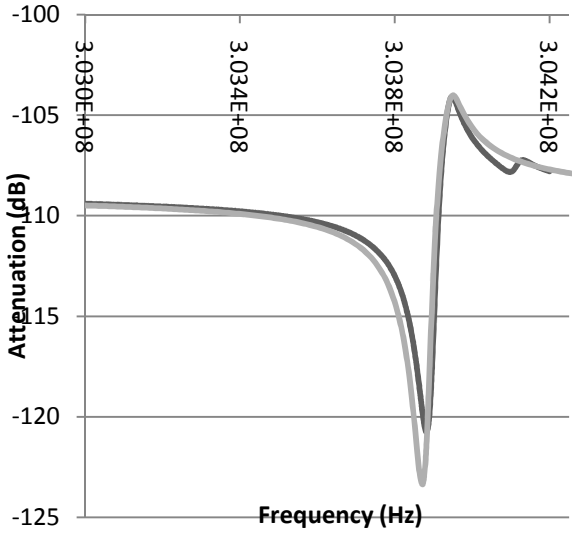

Figure 4-9 : Comparison of measurement (black curve) and simulation results (gray curve) for the impedance of SAW resonator RO2043a.

4.2.2 Narrowband Filter

The performance of the narrowband filter was also measured and simulated both in MATLAB and in Cadence using the equivalent circuit parameters shown in Table 4-3. Figure 4-10 compares results from measurement and simulation of the impedance of a narrowband filter. Here again results are shown in black and simulation results are in gray. The comparison shows good agreement between the theoretical and measured responses.

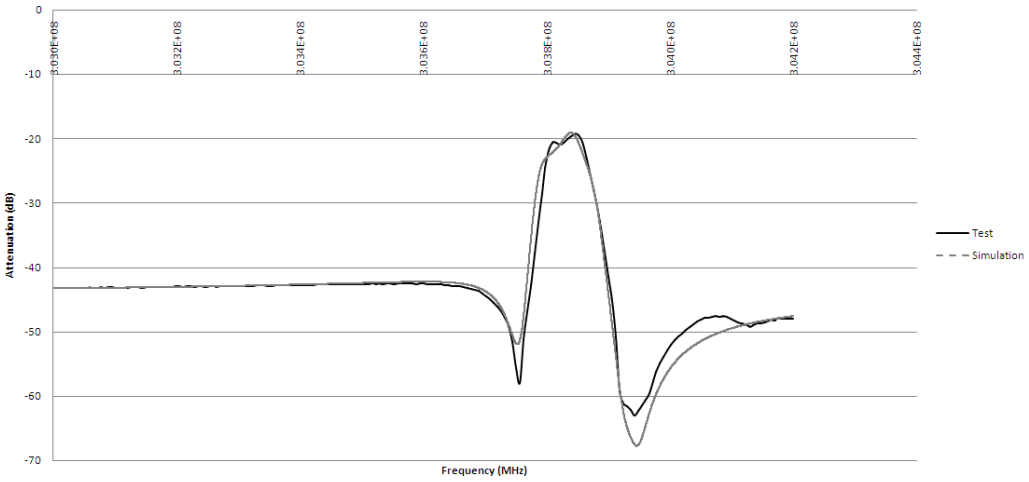

Figure 4-10 : Comparison of results for the 20log(S_{21}) of the narrowband filter (in MHz). Measured data is shown by the black curve and simulation results are shown by the gray curve.

5 Method for Synthesizing Wideband SAW Bandpass Filters

The development of the wideband bandpass filter design was based on a lithium niobate substrate and aluminum electrodes. A basic wideband bandpass filter was designed first using the approach described in Section 3.2. The wideband bandpass design was then altered to force an optimum fit between its response and that of an elliptic *LC* bandpass filter response. The resulting wideband design is currently being fabricated at the (Semiconductor Microsystems Fabrication Laboratory (SMFL) at RIT.

The flowchart for the method of synthesizing a wideband filter and then optimizing it to approach a standard filter function involves many steps. This flowchart, shown in Figure 5-1, is divided into two branches. The first branch defines the standard filter target response while the second branch describes the SAW IEF design. These two branches merge and the standard filter target response and SAW IEF design are entered into a Cadence® optimization routine. The SAW IEF design branch and the standard filter target response branch will be described in detail in Sections 5.1 and 5.2, respectively. The Cadence ® optimization process is described in Section 5.3.

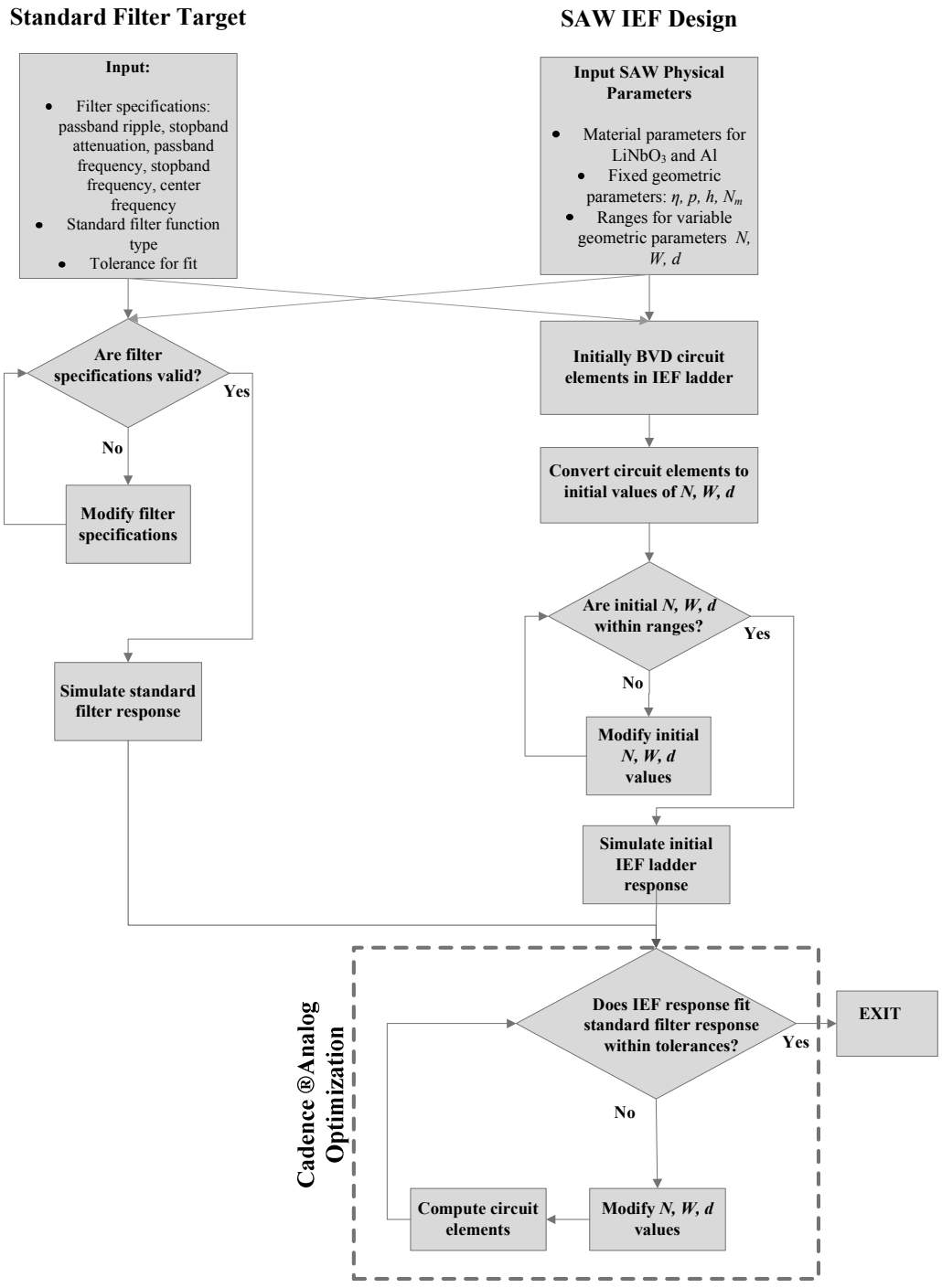

Figure 5-1 : Flowchart describing method for synthesizing and optimizing a wideband IEF network.

5.1 SAW IEF Design

5.1.1 SAW Physical Parameters

In order to find suitable physical parameters to realize this filter response, both material and geometric constraints had to be considered.

Important material parameters of lithium niobate that were needed for the design were: a) the acoustic free wave velocity, v_0, b) the sum of permittivities of the substrate and air, C_s, c) the coupling coefficient, K^2, and d) the characteristic SAW transmission line admittance, y_0. Two material parameters considered for the aluminum electrodes were: a) the density, ρ and b) the reflectance per electrode, r..

There were seven geometric parameters associated with the physical components of the SAW resonator that needed to be specified. These were: a) the electrode pitch, p, b) the metallization ratio, η, c) the distance between the mirror and the IDT, d, d) the thickness of the aluminum electrodes, h, e) the finger overlap, W, f) the number of finger pairs in the mirror, N, and g) the number of fingers in the mirrors, N_m. These geometric parameters were defined assuming the resonators were all symmetric.

For the resonators in the initial wideband filter design, four geometric parameters were assumed to be fixed: η, h, p and N_m. The electrode pitch is related to the acoustic wavelength (see Equation (2-9)) and therefore was fixed for each resonator. The metallization ratio, η, was kept fixed at a value of 0.5. The thickness of the aluminum electrodes was set to be 0.3 µm. Both η and h were chosen since they are convenient values for fabrication. Last of all, the number of fingers in the mirrors, N_m, was assumed

to be equal to 400. This was chosen so that the mirror reflection coefficient would be close to unity, allowing certain assumptions to be made (as described in Section 2.2.4). Using approximate parameters of aluminum and lithium niobate, a reflectance, *r*, of -0.008*i* was computed. The exact value of the mirror coefficient was found to be [14]:

$$|\Gamma_0| = \tanh(N_m|r|) = 0.997 \quad (5\text{-}1)$$

The values of *N*, *W* and *d* were given ranges of values that would be physically realizable with the IC fabrication process used to build these custom resonators. Table 5-1 summarizes these material and geometric considerations.

Table 5-1 : Material and geometric constraints of the wideband SAW IEF designs based on $LiNbO_3$

Material Parameter Values	Geometric Parameters and Ranges
Lithium niobate ($LiNbO_3$)	**Fixed**
v_0=3996 m/s	$p=\lambda_0/2$
C_s=500 pF/m	η=0.5
K^2=0.056	h=0.3 μm
y_0=0.00021 mhos	N_m=400
Aluminum (Al)	**Variable**
ρ=2695 kg/m^3	$10 \le N \le 190$
r=-0.008i	$126\mu m \le W \le 1.8mm$
	$0\lambda_0 \le d \le 90\lambda_0$

5.1.2 Initialization of BVD Circuit Elements

Initial values of BVD circuit elements were based on the three-stage IEF design described by Ikata *et al.* [26]. Lithium niobate was chosen as the piezoelectric substrate because of its high electromechanical coupling coefficient. Furthermore, aluminum was

chosen for the electrode material because of its compatibility with standard tools and processes.

In order to obtain BVD circuit elements, filter specifications were needed. These The were: a) a center frequency of 221.32 MHz, b) passband ripple of less than 0.5 dB, c) stopband attenuation of more than 20 dB, d) a passband frequency of 219.30 MHz, and e) a stopband frequency of 223.35 MHz.

In determining the BVD circuit elements, the impedance matching condition was considered first (see Equation 3-10). From that, it was determined that:

$$C_{Ts}C_{Tp} = \frac{1}{\omega_o{}^2 R^2} = 206.8516(pF)^2 \tag{5-2}$$

It has been demonstrated that the ratio of these transducer capacitances, C_{Tp}/C_{Ts}, is related to both the stopband attenuation and the passband insertion loss of the IEF network [26]. Specifically, greater capacitance ratios offer greater stopband attenuation, but at the expense of insertion loss. A capacitance ratio of 1.5 was imposed on the design in order to have little insertion loss and moderate stopband attenuation. With this ratio and Equation (5-2), the computed transducer capacitances were:

$$\begin{aligned} C_{Ts} &= 11.74313\,pF \\ C_{Tp} &= 17.61469\,pF \end{aligned} \tag{5-3}$$

The series resonant frequency, f_{rs}, and the parallel anti-resonant frequency, f_{ap}, were both designed to be equal to the center frequency of the filter. This satisfies the crucial constraint of IEF networks (Equation 3-1) and also places the frequency overlap in a neutral part of the passband. To realize the desired bandwidth, the parallel resonant frequency was chosen to be 219.30 MHz, while the series anti-resonant frequency was

chosen to be 222.35 MHz. Using Equations (2-4) and (2-5) and the desired resonant and anti-resonant frequencies of the resonators, motional inductances and capacitances were computed as follows:

$$C_{ms} = 0.3748\,pF$$
$$L_{ms} = 2.0697\,\mu H \tag{5-4}$$

$$C_{mp} = 0.2499\,pF$$
$$L_{mp} = 1.4012\,\mu H \tag{5-5}$$

5.1.3 Conversion of Circuit Elements to *N*, *W*, and *d* Values

The computed BVD circuit values (see Equations (5-3) through (5-5)) were used to find relationships between physical parameters for resonators in this initial design using Equations (2-17) through (2-19). It was verified that the computed values of *N*, *W*, and *d* fell within the previously defined ranges (see Table 5-1). These are summarized in the table below.

Table 5-2 : Values of geometric variables in initial wideband design

Series Resonators, Z_s	Parallel Resonators, Z_p
N_s=63 W_s=372.8 μm d_s=80λ_0	N_P=63 W_P=559.2 μm d_P=80λ_{0P}

5.2 Definition of Standard Filter Target

5.2.1 The Elliptic Bandpass Filter Prototype

The standard filter design used as a target for optimization was a sixth-order bandpass *LC* elliptic filter. This order was found necessary to meet the specifications listed in Section 5.1.2. The specification for center frequency of the filter was determined to be the highest VHF center frequency that could be realized given photolithographic considerations of the SMFL. Furthermore, the chosen bandwidth was approximately 4 MHz since it is a reasonable bandwidth for a design based on a lithium niobate substrate (see Figure 2-13). The last specification was for a tolerance of 0.5% for the optimization fit. The *LC* circuit used for the elliptic filter is shown below.

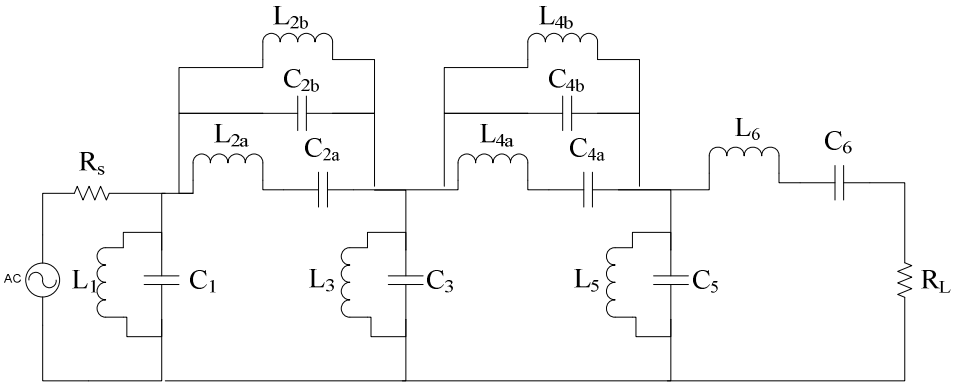

Figure 5-2 : Schematic of *LC* elliptic bandpass filter used as a prototype for optimization

5.3 The Cadence® Optimization Algorithm

The basic wideband bandpass filter was optimized to approach a sixth-order elliptic bandpass filter response using a Cadence® tool named the *optimizer*. This tool is intended for a wide range of applications such as impedance matching in RF circuits,

balancing design tradeoffs, increasing circuit yields, and matching filter frequency responses to filter specifications.

The optimizer can use one of two algorithms to obtain the goal response. These are the LSQ (least square) algorithm and the CFSQP (C version Feasible Sequential Quadratic Programming) algorithm. The LSQ algorithm was chosen since it is more appropriate for filter designs.

The LSQ algorithm includes the following steps: First, the response of the given circuit is simulated using initial values entered by the user when configuring the optimizer. Then the optimizer determines how sensitive the design response is to its variable components. This is accomplished through use of the LSQ algorithm and *Finite Difference Perturbation*, changing variables slightly and re-simulating the response [28]. The optimizer gathers data on the sensitivities of the circuit and uses these to iterate towards a target response. Iterations continue until no more improvement from changing design variables is possible, or when the fit between the two responses meets the tolerance specification.

5.4 Wideband Filter Simulation and Optimization Results

Three simulations were involved in the basic analysis and simulation of the wideband designs. These include the initial wideband bandpass response, the elliptic bandpass response, and also the optimized wideband bandpass response.

5.4.1 Wideband Filter Simulation

The initial wideband bandpass filter design was simulated in Cadence. The circuit components were defined using equations of variables that represent the major physical parameters of interest. This circuit is shown in Figure 5-3.

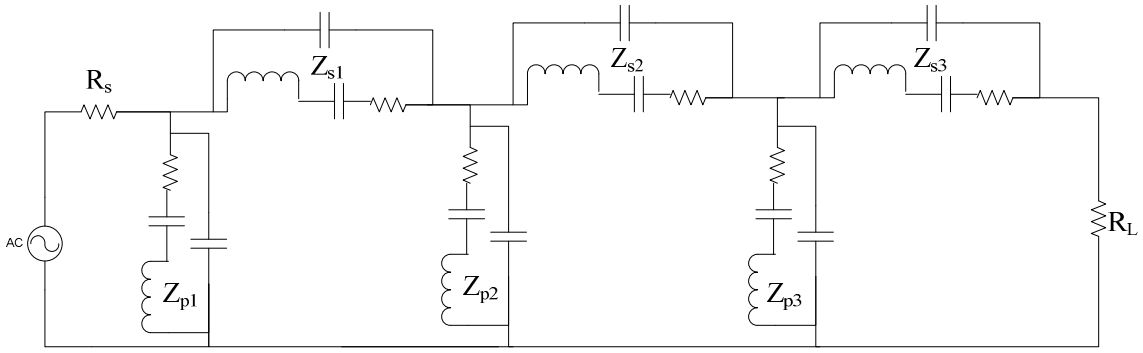

Figure 5-3 : Schematic of wideband IEF design

Simulating this circuit using the physical values found in Table 5-2 yields the response shown in Figure 5-4.

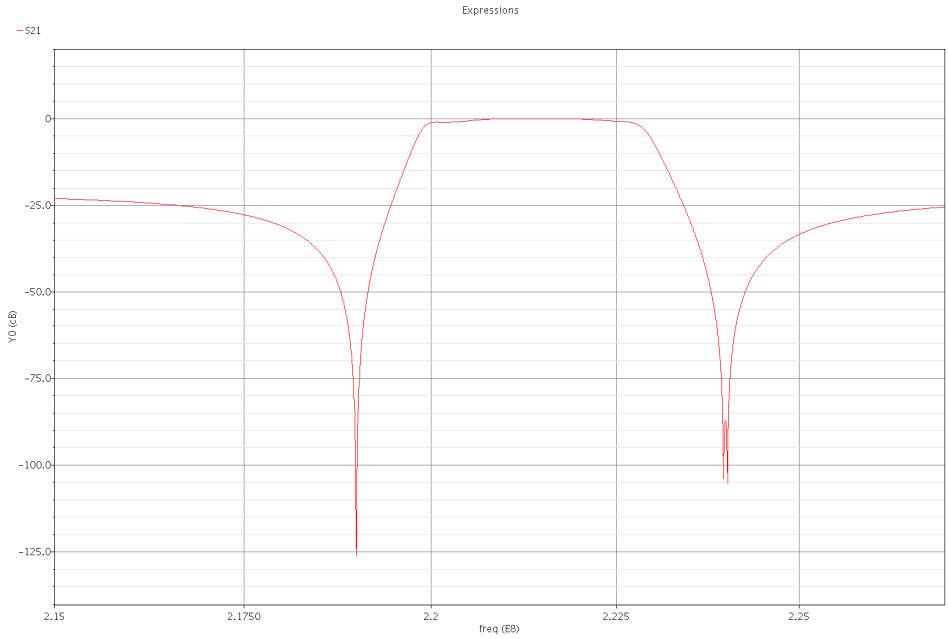

Figure 5-4 : Simulation results for initial wideband IEF design

5.4.2 Elliptic Filter Simulation

The elliptic filter circuit shown in Figure 5-2 was simulated to verify that it met the specifications listed in Section 5.2.1. The results are shown in Figure 5-5.

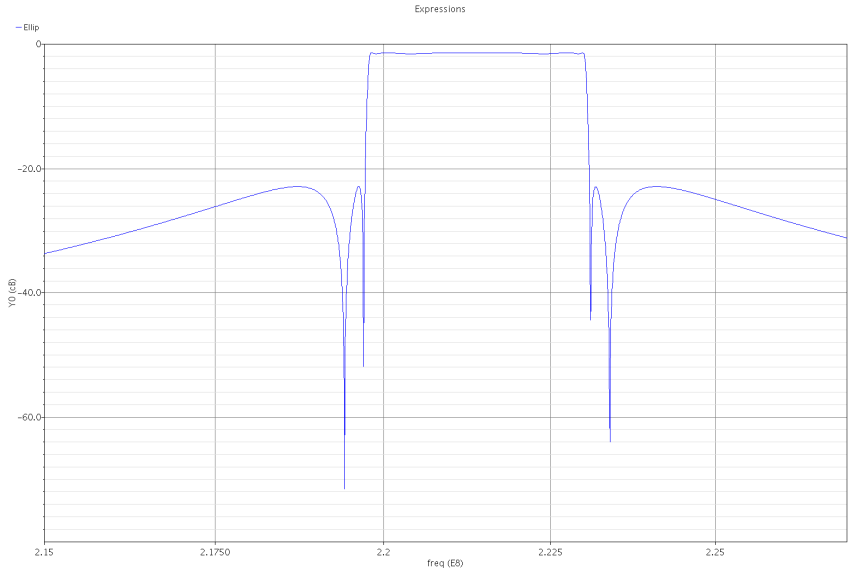

Figure 5-5 : Simulation of target *LC* elliptic bandpass filter design. Specifications are R_p=0.5 dB, R_s=20 dB, Passband 219.8-223 MHz

5.4.3 Wideband Filter Optimization

As previously mentioned, the wideband bandpass filter was optimized with a sixth-order *LC* elliptic bandpass filter. In order for the optimization to yield realistic results, the ranges found in Table 5-2 were included. That way, the physical constraints of fabricating this wideband filter were taken into account in the optimization routine. The final results of the optimization are detailed in Table 5-3.

Table 5-3 : Physical component values for optimized SAW elliptic filter design. Found using a LSQ algorithm in Cadence (0.5% Matching)

Z_{s1}	Z_{s2}	Z_{s3}	Z_{p1}	Z_{p2}	Z_{p3}
N_{s1}=63	N_{s2}=63	N_{s3}=63	N_{p1}=55	N_{p2}=55	N_{p3}=56
W_{s1}=377.6 µm	W_{s2}=374 µm	W_{s3}=374 µm	W_{p1}=426.4 µm	W_{p2}=426.4 µm	W_{p3}=320 µm
d_{s1}=79.74λ_0	d_{s2}=80.24λ_0	d_{s3}=79.78λ_0	d_{p1}=57.86λ_{0P}	d_{p2}=57.86λ_{0P}	d_{p3}=62.19λ_{0P}

The physical layout of Z_{p1}, using the optimized parameters listed in Table 5-3 is illustrated in Figure 5-6. This figure shows the entire resonator layout at the bottom, with an enlarged view of a section of the IDT. The approximate size of this resonator is 10.2 mm x 0.6 mm.

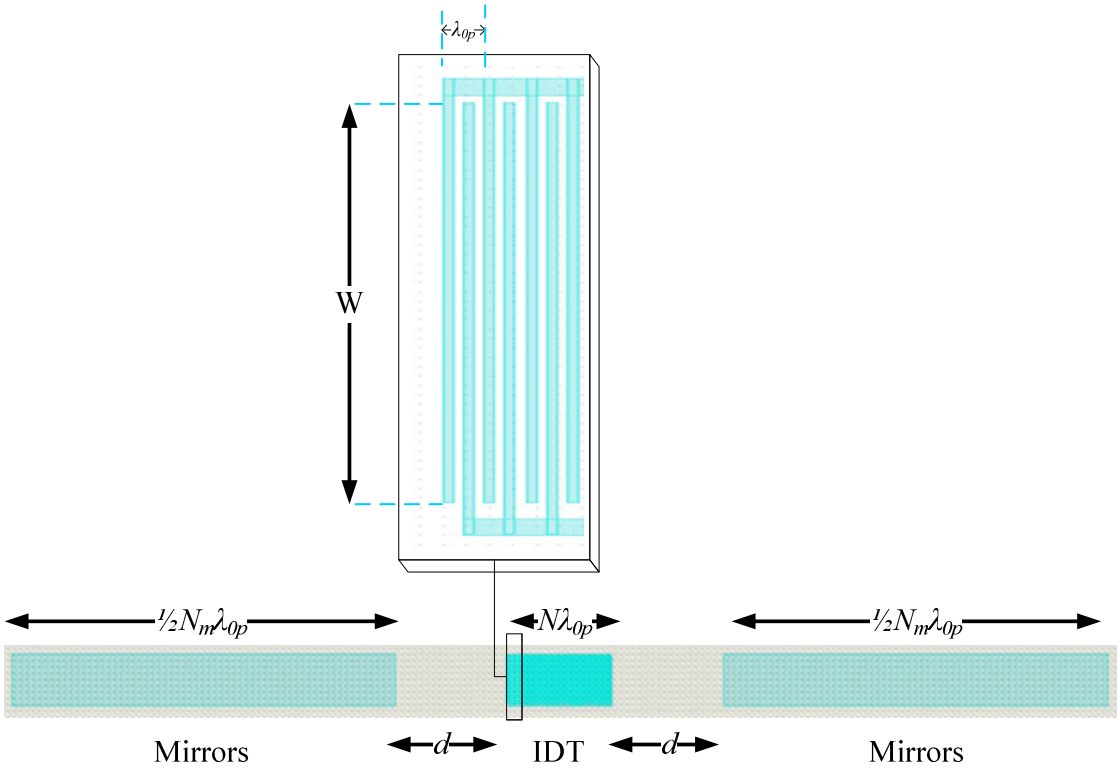

Figure 5-6 : Physical layout of IEF resonator, Z_{p1}. Drawn to scale with enlarged view of an IDT section.

This table also shows that to approach an elliptic response, the series and parallel resonators cannot be identical.

Figure 5-7 shows a comparison of the target elliptic response and the resulting optimized IEF response.

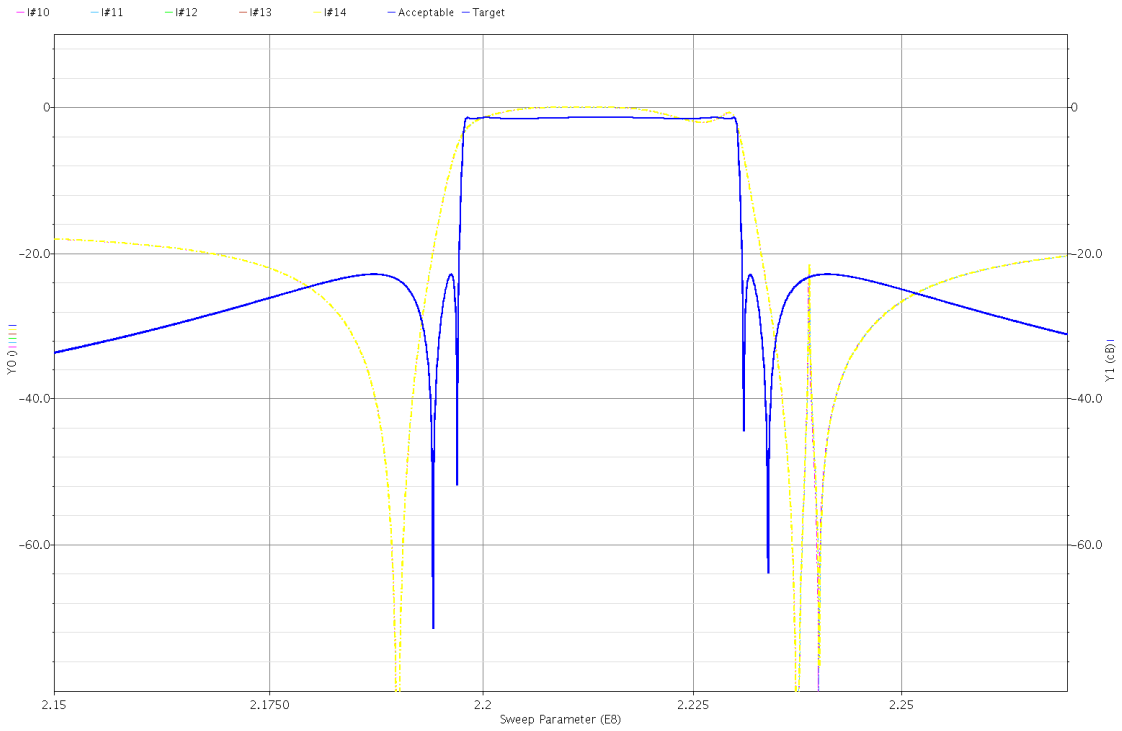

Figure 5-7 : Optimization results. Includes the elliptic *LC* bandpass response (solid line) and also the optimized SAW IEF wideband response (dashed line)

In this figure, the *LC* elliptic bandpass response is denoted by a solid line, while the optimized SAW wideband response is denoted by a dashed line. As can be seen from the above figure, the optimized IEF network realized more than 20 dB of stopband attenuation, less than 2 dB insertion loss and very little passband ripple. Moreover, its passband closely approximates the passband of an elliptic function filter.

6 Conclusions and Future Work

6.1 Conclusions

This work has focused on two main objectives: 1) determining the feasibility of using commercial SAW resonators in narrowband filter designs, and 2) optimizing the fit of wider bandwidth SAW IEF ladder filter responses to standard filter function responses. Many characteristics of SAW devices were exploited to design filters that overcome limitations in both *LC* networks and bulk acoustic wave technology.

It has been shown that the performance of bandpass SAW filters composed of commercial resonators is severely limited, but it is still possible to demonstrate the impedance element filter topology using these resonators. Since all commercial SAW resonators have quartz substrates, the filter response will necessarily have a very narrow bandwidth. Because each commercial resonator is individually packaged, these resonators experience a large insertion loss. This loss increases when the individual resonators are combined to form a filter. However, this insertion loss can be minimized by careful choices in resonator packaging. Even though the commercial resonator filter design presented in Chapter 4 yields large insertion loss and an extremely narrow bandwidth, it still confirms that the IEF topology can be used to realize high *Q* filters that are correct by design and have reasonably good stopband attenuation.

Bandpass IEF SAW filters based on custom-made resonators have fewer constraints and potentially better performance characteristics than commercial IEF SAW filter designs. It was shown that using a black lithium niobate substrate increased the

potential bandwidth of the filter because of its higher electromechanical coupling coefficient, K^2. By considering material and geometric constraints in designing custom SAW resonators, a filter with low insertion loss (<2 dB), a flat passband, and good stopband attenuation was simulated.

The optimization method used for the SAW wideband bandpass design showed that the response function of an IEF topology can be altered to approximate a standard filter response function. Previously SAW filters approaching standard filter functions have only been investigated using apodized transducer filters, not IEF ladder filters. As shown in this work, the optimization routine was able to yield physical parameters that result in SAW IEF ladder response function that approximates an elliptic filter response function. This method provides a means by which SAW bandpass filter designs can be optimized to "fit" standard filter functions, especially in the passband. The advantage of this process is that SAW devices can be used in filter designs to replace conventional inductors and capacitors. In the design example, it was shown that six SAW resonators in an IEF ladder can be used to replace the sixteen inductors and capacitors needed for a sixth-order *LC* elliptic response. Furthermore, this ladder filter design can be fabricated using standard IC fabrication techniques on a single substrate.

6.2 Future Work

The wideband bandpass filter design and optimization technique presented in Chapter 5 can be enhanced in many ways. It was shown that a three-stage (six resonators) IEF topology can approximate an elliptic function that typically has 16 *LC* components. It

is expected that additional IEF stages should result in improved performance. For example, Hashimoto [18] has shown that increasing the number of stages in an IEF network increases the stopband attenuation of the filter. This is illustrated in Figure 6-1. As shown in this figure, the stopband attenuation of *N* stage IEF networks is shown with respect to the transducer capacitance ratio, C_{Tp}/C_{TS}.

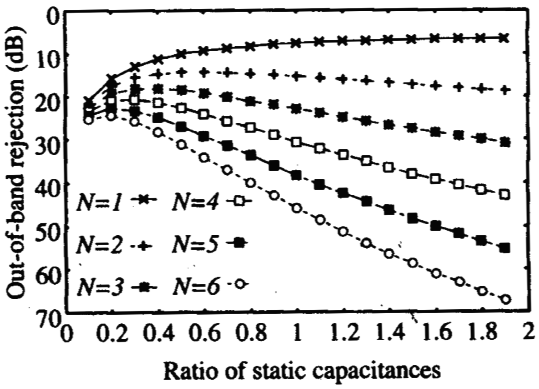

Figure 6-1 : The effects of additional IEF stages and static capacitance ratio on stopband attenuation. Copied from [18]

Wideband SAW IEF designs can also be extended to applications using 75 Ω transmission lines and could potentially offer smaller sized filter designs. As can be seen from Equation 3-9, if the line impedance, *R*, is larger, smaller transducer capacitances are needed. Since transducer capacitance is proportional to *N* and *W*, this could lead to a reduction in overall filter size.

7 Appendix

7.1 S-Parameter Measurements and Calibration

A two-port Agilent Technologies E5071C network analyzer was used for S-parameter measurements of both single commercial quartz resonators and the narrowband ladder network filter based on these resonators. The network analyzer was calibrated using a 7/16 calibration kit and a two-port calibration of shorts, opens, loads and transmission. After calibration, precision 7/16-to-3.5mm and 3.5mm-to-SMA connectors were used to interface with the SMAs mounted on the PCBs. All S-parameters could be easily plotted using the network analyzer. The fundamentals of S-parameter characterization are reviewed in the following paragraphs.

Scattering parameter (or S-parameter) characterization is one of the most useful ways of observing the function of a network. This involves the use of impedance and admittance parameters to convey port voltages in terms of port currents. A typical two-port network is shown below.

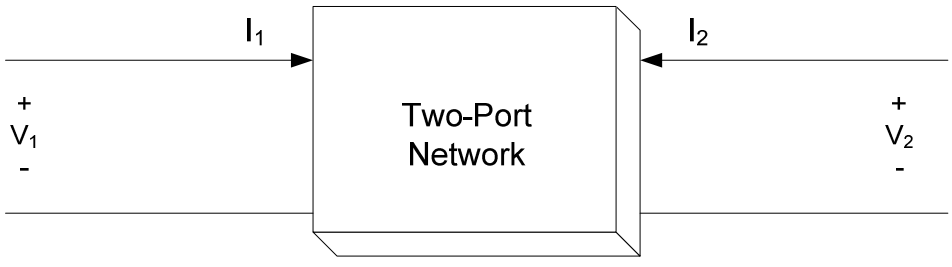

Figure 7-1 : Two-Port Network with Voltage and Current Definitions

For the two-port network shown, the voltage equations are:

$$V_1 = Z_{11} I_1 + Z_{12} I_2 \tag{7-1}$$

$$V_2 = Z_{21} I_1 + Z_{22} I_2 \tag{7-2}$$

Furthermore, the scattering parameters are:

$$S_{11} = \frac{V_1^-}{V_1^+} \tag{7-3}$$

$$S_{12} = \frac{V_1^-}{V_2^+} \tag{7-4}$$

$$S_{21} = \frac{V_2^-}{V_1^+} \tag{7-5}$$

$$S_{22} = \frac{V_2^-}{V_2^+} \tag{7-6}$$

Assuming a passive network, the following relationship exists:

$$Z_{12} = Z_{21} \tag{7-7}$$

7.1.1 S_{21} Transmission of Series and Shunt Devices

This section briefly compares the calculation of the transmission coefficient, or S_{21}, of both a series and parallel impedance. This analysis relies on transmission line theory, using the circuits' transfer functions and voltage transfer relationships.

Figure 7-2 shows the representation of a transmission line with series impedance, including generator source impedance (Z_{source}) and a load impedance (Z_{load}).

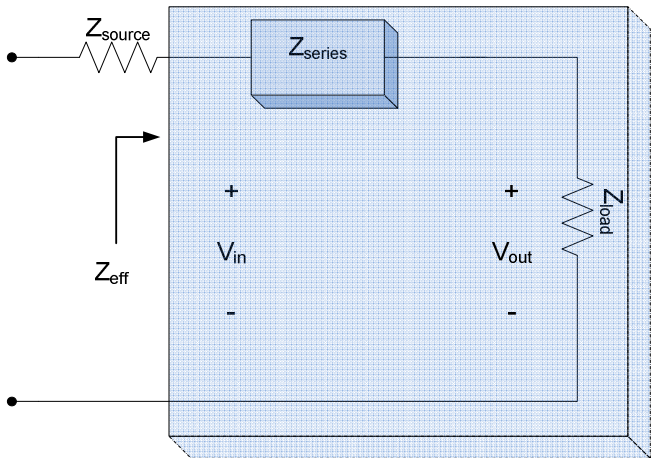

Figure 7-2 : Basic transmission line with added series impedance

S_{21} and S_{11} for the above network are given by:

$$S_{21} = \frac{V_{out}}{V_{in}}(1+\rho) \tag{7-8}$$

$$S_{11} = \rho = \frac{Z_{eff} - Z_{load}}{Z_{eff} + Z_{load}} \tag{7-9}$$

In this case, the transfer function of the network is:

$$T_{ser}(s) = \frac{V_{out}}{V_{in}} = \frac{Z_{load}}{Z_{source} + Z_{series}} \tag{7-10}$$

Assuming the load and source impedances are equal to the characteristic line impedance of the network analyzer, Z_o, this simplifies to:

$$T_{ser}(s) = \frac{V_{out}}{V_{in}} = \frac{Z_o}{Z_o + Z_{series}} \tag{7-11}$$

Furthermore, the effective impedance, Z_{eff}, is equal to:

$$Z_{eff} = Z_{series} + Z_{load} = Z_{series} + Z_o \tag{7-12}$$

Therefore, the S_{21} is found to be:

$$S_{21} = \frac{V_{out}}{V_{in}}(1+\rho) = \frac{Z_o}{Z_o + Z_{series}}\left[\frac{2(Z_{series} + Z_o)}{2Z_o + Z_{series}}\right] = \frac{2Z_o}{2Z_o + Z_{series}} \tag{7-13}$$

Figure 7-3 shows the network representation for a transmission line with shunt impedance.

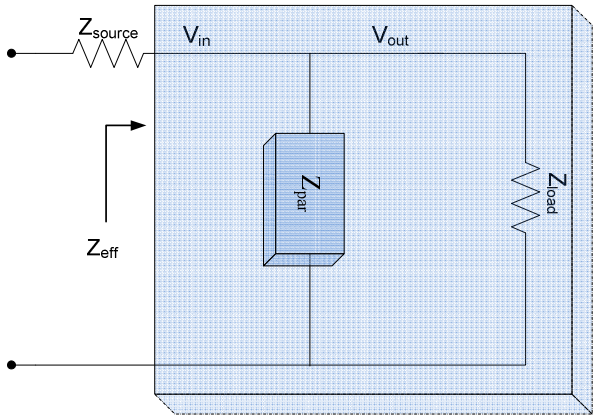

Figure 7-3 : Basic transmission line with added parallel impedance

In the case of parallel impedance, the input voltage is equal to the output voltage, as shown in the above figure. Thus, the transfer function of this network is equal to one. Once again, assuming that the source and load impedances are equal to Z_o, the effective impedance, Z_{eff}, is equal to:

$$Z_{eff} = \frac{Z_o Z_{par}}{Z_o + Z_{par}} \tag{7-14}$$

S_{11} is given by:

$$S_{11} = \rho = \frac{Z_{eff} - Z_{load}}{Z_{eff} + Z_{load}} = \frac{-Z_0{}^2}{Z_0{}^2 + 2Z_0 Z_p} \tag{7-15}$$

Therefore, the S_{21} is simplified to:

$$S_{21} = \frac{V_{out}}{V_{in}}(1+\rho) = \frac{2Z_o Z_{par}}{Z_o{}^2 + 2Z_o Z_{par}} = \frac{2Z_{par}}{Z_o + 2Z_{par}} \tag{7-16}$$

7.2 Characterization of a Single SAW Resonator

Characterization of single surface acoustic wave devices is vital in the physical design process since it ensures proper configuration and operation of the devices. As previously stated, the Butterworth Van-Dyke Model allows for more useful (and less complex) parameter extraction. Recall, the expression for the general impedance of a single Butterworth Van-Dyke circuit is:

$$Z_{BVD} = \frac{1}{sC_T}\frac{s^2 L_m C_m + sR_m C_m + 1}{s^2 L_m C_m + sR_m C_m + (1 + C_m/C_T)} \tag{7-17}$$

At the frequency of series resonance, the impedance is:

$$Z_{BVD}(\omega_s) = \frac{1}{j\omega_s C_T}\frac{j\omega_s R_m/L_m}{-\omega_s{}^2 + j\omega_s R_m/L_m + \omega_s{}^2(1 + C_m/C_T)} \tag{7-18}$$

At the frequency of parallel resonance, the impedance is:

$$Z_{BVD}(\omega_p) = \frac{1}{j\omega_p C_T}\frac{-\omega_p{}^2 + j\omega_p R_m/L_m + \dfrac{\omega_p{}^2}{(1 + C_m/C_T)}}{j\omega_p R_m/L_m} \tag{7-19}$$

To define ω_p and ω_s in Equations 7-18 and 7-19, the following two relationships are used:

$$\omega_s = \sqrt{\frac{1}{L_m C_m}} \tag{7-20}$$

$$\omega_p = \sqrt{\frac{C_m + C_T}{L_m C_m C_T}} = \omega_s \sqrt{1 + \frac{C_m}{C_T}} \tag{7-21}$$

With the above relationships, taking the magnitudes of both sides of Equations 7-18 and 7-19 yield:

$$\left|Z_{BVD}(\omega_s)\right| = \left|\frac{R_m}{j\omega_s R_m C_T + 1}\right| \cong R_m \tag{7-22}$$

$$\left|Z_{BVD}(\omega_p)\right| = \left|\frac{1 - j\omega_p R_m C_T}{{\omega_p}^2 R_m {C_T}^2}\right| \cong \frac{1}{{\omega_p}^2 R_m {C_T}^2} \tag{7-23}$$

Extraction of values for R_m, L_m, C_m and C_T is obtained from four main equations. The first two equations (7-20) and (7-21) show the relationship between the resonant and anti-resonant frequencies and the equivalent circuit parameters. Moreover, the other equations (7-22) and (7-23) relate the maximum and minimum measured impedances to the equivalent circuit parameters and are obtained from the previous two equations. Note that the impedance at the frequency of series resonance is at a minimum, while the impedance at the frequency of parallel resonance is at a maximum.

The equation for the shunt capacitance, C_T, is found from (7-22) and (7-23):

$$C_T \cong \sqrt{\frac{1}{{\omega_p}^2 \left[Z_{BVD}(\omega_s)\right]\left[Z_{BVD}(\omega_p)\right]}} \tag{7-24}$$

The equation for the motional inductance, L_m, is found from (7-20) and (7-21):

$$L_m = \frac{1}{C_T(\omega_p{}^2 - \omega_s{}^2)} \tag{7-25}$$

Finally, the equation for the motional capacitance, C_m, is found from (7-19):

$$C_m = \frac{1}{L_m \omega_s{}^2} \tag{7-26}$$

7.3 MATLAB Code for Parameter Extraction of BVD Equivalent Circuit Parameters

```
%   EquivBVD.m              Created by Melissa Dempsey on June 15,
2009

%   This code is to be used to find the equivalent circuit
parameters of a
%   SAW resonator using its S21 response from a network analyzer.
This is
%   accomplished through four careful measurements: maximum S21,
minimum
%   S21, and the two frequencies these occur at.

%   A maximum S21 corresponds to a minimum impedance, thus a maximum
S21
%   occurs at the frequency of series resonance. Likewise, a minimum
S21
%   occurs at the frequency of parallel resonance.

format long e
P=bodeoptions;
P.FreqUnits='Hz';       % Sets the frequency units to Hz

Smax_dB=input('\nWhat is the maximum magnitude, in dB, of the S21?
'); % This should always be a negative value
Smax=10^(-Smax_dB/20);

Smin_dB=input('\nWhat is the minimum magnitude, in dB, of the S21?
'); % This should always be a negative value
Smin=10^(-Smin_dB/20);

Zmin=(100-(100*Smax))/(Smax);          % Computes the maximum
impedance
```

```
Zmax=(100-(100*Smin))/(Smin);           % Computes the minimum
impedance

fs=input('\nWhat is the frequency, in MHz, at which the maximum
magnitude of S21 occurs? ');
ws=2*pi*fs*1e6;

fp=input('\nWhat is the frequency, in MHz, at which the minimum
magnitude of S21 occurs? ');
wp=2*pi*fp*1e6;

Rm=Zmin
Co=sqrt((wp*wp*Zmin*Zmax)^-1)
Lm=(Co*((wp*wp)-(ws*ws)))^-1
Cm=(Lm*ws*ws)^-1

num_Zbvd=(1 Rm/Lm 1/(Lm*Cm));                   % Calculates and
plots the impedance of the SAWR
den_Zbvd=(Co (Rm*Co)/Lm ((Cm+Co)/(Lm*Cm)) 0);
Zbvd=tf(num_Zbvd,den_Zbvd);

subplot(1,2,1)
bode(Zbvd,{(0.9*ws) (1.1*ws)},P)
grid on
title('Impedance of SAWR')


S21=100/(100+Zbvd);                             % Calculates and
plots the S21 of the SAWR
subplot(1,2,2)
bode(S21,{(0.9*ws) (1.1*ws)},P)
grid on
title('S21 of
```

8 Bibliography

[1] A. B. Williams, *Electronic Filter Design Handbook*. McGraw-Hill Publishing Company, 1988.

[2] M. Puckette, "Filters," in *The Theory and Technique of Electronic Mus.* Singapore: World Scientific Publishing Co., 2007.

[3] O. Heaviside, *Electrical Papers*. London : Macmillan, 1892, vol. 1.

[4] K. W. Wagner, "Spulen- und Kondensatorleitungen," *Archiv fur Elektrotechnik*, pp. 61-92, 1919.

[5] G. A. Campbell, "Electric wave-filter," US Patent 1,227,113, Jul. 15, 1915.

[6] O. J. Zobel, "Theory and Design of Uniform and Composite Electric Wave Filters," *Bell Telephone Syst. Tech.*, vol. 2, no. 1, 1923.

[7] Kerry Lacanette. (1991, Apr.) A Basic Introduction to Filters--Active, Passive, and Switched-Capacitor. [Online]. http://www.national.com/an/AN/AN-779.pdf

[8] G. A. Campbell, "Physical Theory of the Electric-Wave Filter," *Bell Sys. Tech.*, vol. 1, no. 2, pp. 1-32, 1922.

[9] R. Schaumann and M. E. Van Valkenburg, *Design of Analog Filters*. Oxford University Press, 2001.

[10] P. Hartemann and E. Dieulesaint, "Acoustic-surface-wave filters," vol. 5, pp. 657-658, Dec. 1969.

[11] Tancrell, R. H., "Analytic Design of Surface Wave Bandpass Filters," vol. SU-21, pp. 12-22, 1974.

[12] L. A. Coldren and R. L. Rosenberg, "Surface-acoustic-wave resonator filters," *Proceedings of the IEEE*, vol. 67, no. 1, pp. 147-158, Jan. 1979.

[13] V. M. Ristic, *Principles of Acoustic Devices*. Toronto, Canada: John Wiley & Sons, 1983.

[14] S. Datta, *Surface Acoustic Wave Devices*, S. Papanikolaou, Ed. Englewood Cliffs, NJ, USA: Prentice-Hall, 1986.

[15] C. Campbell, *Surface Acoustic Wave Devices and Their Signal Processing Applications*. Academic Press, INC, 1989.

[16] V. K. Varadan, K. J. Vinoy, and K. A. Jose, *RF MEMS and Their Applications*. John Wiley & Sons LTD, 2003.

[17] R. Krishnan, H. B. Nemade, and R. Paily, "Simulation of One-Port SAW Resonator using COMSOL Multiphysics," in *COMSOL Users Conference 2006 Bangalore*, Guwahati, 2006.

[18] K.-Y. Hashimoto, *Surface Acoustic Wave Devices in Telecommunications*. Springer,

2000.

[19] Hashimoto, *IEEE Transactions on Ultrasonics, Ferroelectrics, and Frequency Control*, vol. 51, no. 11, pp. 1394-1403, Nov. 2004.

[20] G. G. Yaralioglu, A. S. Ergun, B. Bayram, E. Haeggstrom, and B. T. Khuri-Yakub, "Calculation and Measurement of Electromechanical Coupling Coefficent of Capacitive Micromachined Ultasonic Transducers," *IEEE Transactions on Ultrasonics, Ferroelectrics, and Frequency Control*, vol. 50, no. 4, pp. 449-456, 2003.

[21] H. Yatsuda, T. Inaoka, and T. Horishima, "IIDT Type Low-Loss SAW Filters with Improved Stopband Rejection in the Range of 1 to 2 GHz," *IEEE Ultrasonics Symposium*, 1992.

[22] D. P. Morgan, "A History of SAW Devices," in *Advances in Surface Acoustic Wave Technology, Systems and Applications*. Singapore: World Scientific Publishing, 2000, p. 11.

[23] D. P. Morgan, "Surface Acoustic Wave Devices," in *Handbook of Microwave Components and Engineering*, K. Chang, Ed. Hoboken, NJ: John Wiley & Sons, Inc., 2003.

[24] C. C. W. Ruppel, *Advances in Surface Acoustic Wave Technology, Systems and Applications*. World Scientific Publishing Company, 2000.

[25] C. W. Ruppel, et al., "SAW Devices for Consumer Applications," *IEEE Trans. Ultrason., Ferroelec., Freq. Contr.*, vol. 40, pp. 438-452, 1993.

[26] O. Ikata, T. Miyashita, T. Matsuda, T. Nishihara, and Y. Satoh, *IEEE Ultrasonics Symp.*, pp. 111-115, 1992.

[27] RF Monolithics, Inc. (2009) RFM. [Online]. http://www.rfm.com/products/spec_sheet.php?record=RO2043

[28] Cadence, "Cadence(R) Advanced Analysis Tools User Guide," 2002.